

Fault friction under thermal pressurization during large coseismic-slip

Part II: Expansion to the model of frictional slip

Alexandros Stathas^a, Ioannis Stefanou^{a,*}

^a*Institut de Recherche en Génie Civil et Mécanique (UMR CNRS 6183), Ecole Centrale de Nantes, Nantes, France*

Abstract

In Stathas and Stefanou (2022) we presented the frictional response of a bounded fault gouge under large coseismic slip. We did so by taking into account the evolution of the Principal Slip Zone (PSZ) thickness using a Cosserat micromorphic continuum model for the description of the fault's mechanical response. The numerical results obtained differ significantly from those predicted by the established model of thermal pressurization during slip on a mathematical plane (see Mase and Smith (1987); Rice (2006a); Platt et al. (2014a) among others). These differences prompt us to reconsider the basic assumptions of a stationary strain localization on an unbounded domain present in the original model. We depart from these assumptions, extending the model to incorporate different strain localization modes, temperature and pore fluid pressure boundary conditions. The resulting coupled linear thermo-hydraulic problem, leads to a Volterra integral equation for the determination of fault friction. We solve the Volterra integral equation by application of a spectral collocation method (see Tang et al. (2008)), using Gauss-Chebyshev quadrature for the integral evaluation. The obtained solution allows us to gain significant understanding of the detailed numerical results of Part I. We investigate the influence of a traveling strain localization inside the fault gouge considering isothermal, drained boundary conditions for the bounded and unbounded domain respectively. We compare our results to the ones available in Lachenbruch (1980); Lee and Delaney (1987); Mase and Smith (1987) and Rice (2006a). Our results establish that when a stationary strain localization profile is applied on a bounded domain, the boundary conditions lead to a steady state, where total strength regain is achieved. In the case of a traveling instability such a steady state is not possible and the fault only regains part of its frictional strength, depending on the seismic slip velocity and the traveling velocity of the shear band. In this case frictional oscillations increasing the frequency content of the earthquake are also developed. Our results indicate a reappraisal of the role of thermal pressurization as a frictional weakening mechanism.

Keywords: strain localization, traveling instability, traveling waves, thermal pressurization, spectral method, Green's kernel

1. Introduction

The results of Part I (see Stathas and Stefanou, 2022), concerning the influence of the weakening mechanism of thermal pressurization, diverge -spectacularly- from the expected behavior based on the model of Mase and Smith (1987); Rice (2006a). Furthermore, we note that these results, indicate the divergence to take place long before the completion of the seismic slip δ . This holds true for the range of commonly observed seismic slip velocities $\dot{\delta} \in \{0.1 \sim 1\}$ m/s and seismic slip displacements $\delta \in \{0.1 \sim 1\}$ m (see Harbord et al. (2021); Rempe et al. (2020)). In this follow-up paper, Part II, we investigate the reasons for this divergence between the theoretical results and their implications for the appreciation of thermal pressurization as one of the main weakening mechanism during coseismic slip. Our investigation leads us to extend the existing model of slip on a mathematical plane by relaxing its key assumptions.

In Figure 1 we compare the frictional response of the micromorphic model used in Part I (see Stathas and Stefanou, 2022), with the response of the established model for the limiting cases of uniform shear Lachenbruch (1980) and shear on a mathematical plane Mase and Smith (1984); Rice (2006a). In particular, the two limiting responses of the established model, depend on the width of accumulating strain

*Corresponding author

Email address: ioannis.stefanou@ec-nantes.fr (Ioannis Stefanou)

localization inside the fault gouge, which we call the Principal Slip Zone (PSZ). They are characterized respectively by: a) the uniform slip across the fault gouge (see Lachenbruch (1980)), and b) the localization of slip on a mathematical plane (see Lee and Delaney (1987); Mase and Smith (1987); Rempel (2006); Rice (2006a)). We note that while at the initial stages of slip (see inset of Figure 1) the response of the micromorphic model lies inside the the envelope of the limit cases, at larger values of slip it diverges, presenting frictional regain and the initiation of frictional oscillations. These results come in contrast to the strictly monotonous behavior predicted by the limiting cases of uniform slip and slip on a mathematical plane.

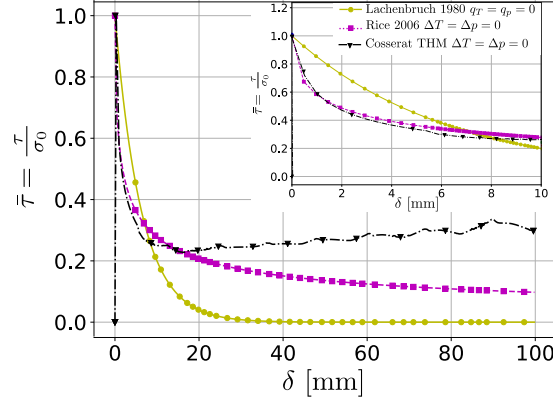


Figure 1: Comparative normalized friction $\bar{\tau}$ - displacement δ results. The purple-square curve presents the frictional response of the established thermal pressurization model in the case of slip on a mathematical plane under isothermal drained boundary conditions lying at infinity Mase and Smith (1987); Rice (2006a). The yellow-circle curve presents the frictional response of the established model when uniform slip occurs under adiabatic undrained boundary conditions for a fault gouge of height $H=1$ mm under shear velocity $V=1$ m/s Lachenbruch (1980). The black-triangle line corresponds to the frictional response of the micromorphic model of Part I, Stathas and Stefanou (2022) for the same fault gouge under isothermal drained boundary conditions. For small values of slip $\delta \leq 10$ mm, the response of the micromorphic model lies between the two limiting cases, however, it diverges as seismic slip δ accumulates.

We note here, that the limiting cases are predicted by the established model of thermal pressurization, under three important assumptions (see Lachenbruch (1980); Mase and Smith (1987); Rice (2006a)): First of all, the thickness of the yielding region, which corresponds to the PSZ, coincides with the fault gouge. Prescribing the thickness, and therefore, the shape of plastic strain profile, essentially decouples the mechanical and thermo-hydraulic components of the coupled THM problem (see Mase and Smith (1984)). Secondly, the variability between the thermal and hydraulic parameters of the gouge and the surrounding rock is assumed to be small, thus the thermo-hydraulic boundaries for the THM coupled problem lie at infinity. In essence the change of hydrothermal parameters between the fault gouge and the surrounding rock is neglected. Lastly, the position of the heat source due to the dissipation inside the PSZ, remains stationary inside the fault, and coincides to the position of the fault gouge.

These assumptions, however, are not representative of observations. We know from laboratory experiments and in situ observations that the fault gouge, has a finite thickness of the order of some millimeters, and it does not deform in a uniform manner (see Myers and Aydin (2004); Brantut et al. (2008)). In fact, inside the fault gouge, the principal slip zone (PSZ) is a region of finite thickness of the order of some micrometers depending on the geomaterial's microstructure (see Muhlhaus and Vardoulakis (1988); Sibson (1977)). In this configuration the fault gouge and the region that accumulates the majority of the plastic deformation inside it -the PSZ- do not coincide. Furthermore, one needs to acknowledge, that the frictional response inside the fault gouge is dependent on the ratio of thermal to hydraulic diffusivity of the fault gouge and the surrounding rock. In particular we know from the works of Aydin (2000); Passelègue et al. (2014); Yao et al. (2016) that the hydraulic and thermal diffusivity of the gouge is smaller than that of the surrounding rock by 1 to 2 orders of magnitude. This large difference between the parameters of the fault system needs to be accounted for. Finally, there is experimental evidence of fault gouges, that are thicker than expected according to the existing models of Platt et al. (2014a) and Rice (2006a), and of closely adjacent fault gouges, see Nicchio et al. (2018), whose existence can be linked to the possibility that the position of the PSZ is not stationary, rather it is traveling inside the fault gouge, possibly expanding the latter in the process.

There is also theoretical evidence considering the possibility of a traveling PSZ inside the fault gouge. In

this case the preferred mode of strain localization might not be that of the divergence kind described in Rice (1975), rather it can be a “flutter” type instability, corresponding to a traveling strain localization profile (PSZ). According to the Lyapunov theory of stability (see Lyapunov (1893); Brauer and Nohel (1969)), a traveling strain localization (PSZ) is manifested by the appearance of a Lyapunov exponent with imaginary parts. The transition from a stationary instability of divergence type to a flutter traveling instability is called a Hopf bifurcation. For more details we refer to section ?? of Part I, Stathas and Stefanou (2022), where we have shown numerically that, for stress states common in faults, traveling instabilities are present in the linear stability analysis for Cosserat continua under strain softening and apparent softening due to multiphysical couplings. In the broader context of a classical continuum, under hydraulic couplings, Benallal and Comi (2003) have shown that traveling instabilities are also present. It is not yet clear if this is the case for a classical continuum under THM couplings (see Benallal (2005)).

In this paper we provide an explanation concerning the differences between the numerical results of Part I (see Stathas and Stefanou (2022)) and the frictional response predicted by limit cases of the classical model Lachenbruch (1980); Mase and Smith (1987); Rice (2006a). To this end we expand the classical model of thermal pressurization described in Rice (2006a), and extend its applicability to cases of bounded fault gouges and traveling strain localization modes of the PSZ. We will use the same thermal, hydraulic and geometric parameters for the fault gouge as in the model of Part I, Stathas and Stefanou (2022). Next, we will collapse the PSZ, where yielding and frictional heating takes place, onto a mathematical plane by employing the same formalism used in Lee and Delaney (1987); Mase and Smith (1987); Rice (2006a). We assume further, that the yield (dissipation) obeys a Coulomb friction law with the Terzaghi normal effective stress. The mechanical behavior of the layer outside the yielding plane is ignored and for the purposes of this model it can be considered as rigid. This allows us to avoid solving a BVP for the mechanical part, which significantly simplifies the problem (c.f. Stathas and Stefanou (2022)).

The decision to collapse the PSZ onto a mathematical plane can be justified based on the results of Part I, see sections ??, ?? and Figures ??,??). These lead us to the observation that it is the hydraulic and thermal parameters of the fault that mainly affect thermal pressurization. We note, however, that the Cosserat radius, which is a parameter connected with the grain size and the material properties of the granular medium is still an indispensable internal length for the numerical analyses of Part I because: a) it assures the mesh independence of the numerical results, and b) it provides finite localization width over which frictional heating takes place. However, for the analyses performed in this part (Part II), the introduction of the Dirac delta distribution prescribing the profile of the plastic strain rate, thus decoupling the mechanical and thermohydraulic component of the problem of thermal pressurization, allows us to overcome the problem of incorporating the microstructure to the model, considerably simplifying the analysis. This allows us to elaborate on the effect of the boundary conditions on the frictional response. Furthermore, this simplification allows us to gain further insight into the problem, because the mechanisms responsible for the principal characteristics of the response of the micromorphic model described in Part I (restrengthening, frictional oscillations) can be isolated and investigated separately, corroborating the numerical results of Part I.

This paper is structured as follows: In section 2 we present the basic equations of the classical model of thermal pressurization (see Mase1987,Mase1984,Rice2006) and our proposed expansion to the cases of bounded fault gouges and a traveling PSZ, by elaborating further on their differences. Our extended model leads to a Volterra integral equation of the second kind, which cannot be solved analytically as in the case of Rice (2006a). In section 3, we solve the Volterra integral equation of the second kind by applying a Spectral Collocation Method with Lagrange basis functions (SCML), based on the work of Evans et al. (1981); Elnagar and Kazemi (1996); Tang et al. (2008). This is a general spectral method and can handle the challenging task of integrating the Volterra equation under different assumption of boundary conditions and traveling strain localization modes, when other analytical approaches such as Laplace transform, Adomian decomposition Method and Taylor series expansion fail (see Wazwaz, 2011; Boyd, 2006).

Having described our model and the solution procedure, we present in section 4 a series of applications showcasing the differences with the analyses in Rice (2006a). The applications include the frictional responses of: (a) a stationary PSZ on a bounded isothermal drained domain, (b) a moving PSZ on an unbounded isothermal drained domain, and (c) a moving PSZ on a bounded isothermal drained domain.

The original solution in Rice (2006a) is obtained as a special case of the more general solutions presented here and is taken as reference (see Figure 3).

Finally, in conclusions we discuss the implications of our results concerning the introduction of a traveling PSZ inside the fault gouge. Our results are important as they describe better the underlying physical process of seismic slip. Moreover, a traveling PSZ naturally enhances the frictional response with oscillations, which in turn can enhance the ground acceleration spectra with higher frequencies as observed in nature Aki (1967); Brune (1970). Moreover, our results are valuable in the context of experiments for the description of the weakening behavior due to thermal pressurization (see Badt et al. (2020)), for controlling the transition from steady to unsteady slip and for the nucleation of an earthquake (see Rice (1973); Viesca and Garagash (2015)). They are also central in earthquake control, as they provide bounds for the apparent friction coefficient with slip and slip-velocity enabling modern control strategies (see Stefanou (2019); Stefanou and Tzortzopoulos (2020); Tzortzopoulos (2021)).

2. Thermal pressurization model of slip on a plane

2.1. Problem statement

We already discussed in the introduction, that the current model of thermal pressurization, shown in Figure 2, assumes that yielding is constrained on a mathematical plane inside the domain, which is modeled based on the Coulomb friction criterion (see equation (3) below). This plane will be also called yielding plane in the following. Contrary to Mase and Smith (1987); Rice (2006a)), the yielding plane is not considered stationary inside the domain. Instead its position $u(t)$ is allowed to change with a velocity $\dot{u}(t) = v(t)$. Furthermore, we will not consider only isothermal drained boundary conditions lying at infinity. In particular, we will also take into account the case, where the fault gouge is bounded under isothermal drained boundary conditions lying at $y = 0$ $y = H$.

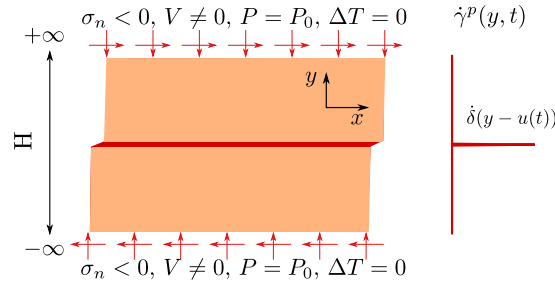


Figure 2: The established model of thermal pressurization: The values of Pressure and temperature are prescribed at infinity. The bodies outside the fault gouge (red color) are considered rigid. Deformation localizes on a mathematical plane and the PSZ coincides with the fault gouge.

At the yielding region inside the layer heat is produced due to dissipation, D . The thermal source then is described by the calculation of the plastic work rate, \dot{D} , at the position of the failure plane, namely:

$$\dot{D} = \tau(t)\dot{\gamma}^p(y, t). \quad (1)$$

In the above formula, friction $\tau(t)$, which is the main unknown of the problem, is independent of position y , due to equilibrium considerations along the height of the fault gouge ($\frac{\partial \tau}{\partial y} = 0$, in the absence of inertia, see also Rice (2006a)). The term $\dot{\gamma}^p(y, t)$ is the plastic strain rate inside the fault gouge. In the established model of thermal pressurization this term is prescribed with the help of a Dirac distribution stationed at the plane of symmetry, $y = 0$ (see Mase and Smith (1984); Rice (2006a)). Here we expand the term $\dot{\gamma}^p(y, t)$ to account for a traveling PSZ at position $y = u(t)$ as follows:

$$\dot{\gamma}^p(y, t) = V(t)\delta_{\text{Dirac}}(y - u(t)). \quad (2)$$

In the case of $u(t) = 0$, no traveling can take place and the stationary condition of Mase and Smith (1987); Rice (2006a) is recovered. In the model of Rice (2006a) the author considers that the shear rate $V(t)$ applied at the boundaries of the fault gouge is constant $V(t) = V$. We adopt this assumption although seismic slip rate during coseismic slip may vary significantly (see Rempe et al. (2020)). The

equations of the established model Mase and Smith (1987); Rice (2006a) are then written as follows:

$$\tau(t) = f(\sigma_n - P_{max}(t)), \text{ on the yielding plane,} \quad (3)$$

$$\frac{\partial \Delta T}{\partial t} = c_{th} \frac{\partial \Delta T}{\partial y^2} + \frac{1}{\rho C} \tau(t) V \delta_{\text{Dirac}}(y - u(t)), \quad (4)$$

$$\frac{\partial \Delta P}{\partial t} = c_{hy} \frac{\partial \Delta P}{\partial y^2} + \Lambda \frac{\partial \Delta T}{\partial t}, \quad (5)$$

$$\Delta T|_{y=0,H} = \Delta P|_{y=0,H} = 0, \quad (6)$$

$$\Delta T(y, 0) = \Delta P(y, 0) = 0, \quad P(y, t) = \Delta P(y, t) + P_0, \quad (7)$$

where f is the friction coefficient, c_{th} , c_{hy} are the thermal and hydraulic diffusivity of the layer (same values for the fault gouge and the fault walls) respectively, ρC is the specific heat density of the layer, V is the shearing rate of the layer, assumed here to be constant, and $\Lambda = \frac{\lambda^*}{\beta^*}$ is the thermal pressurization coefficient (see Table 1). The symbol $(\|_\alpha)$ indicates the value of temperature and pressure fields at position α of the model, while P_0 is the ambient value of pore fluid pressure at the boundaries of the fault gouge. We note that if we set the boundary conditions at infinity (i.e. $\|_{\pm\infty}$) the boundary assumptions of Mase and Smith (1987) and Rice (2006a) are recovered.

We note here, that prescribing the position of the yielding plane $y = u(t)$ implies that the position of P_{max} is known, and coincides with the position of the thermal load. Thus the above model is valid if the position of the maximum pressure $P_{max}(t)$ and the yielding plane coincide. In this case, because the yielding position is prescribed and the plastic strain profile known, the mechanical behavior is decoupled and the resulting coupled thermo-hydraulic problem described above is linear.

Applying the pore fluid pressure solution (see also equation (A.8) in Appendix A) to the failure criterion results finally to the following Volterra integral equation of the second kind for the determination of the layer's frictional response under constant shearing rate (see Rice (2006a); Wazwaz (2011)):

$$\tau(t) = f(\sigma_n - P_0) - \frac{f\Lambda V}{\rho C(c_{hy} - c_{th})} \int_0^t \tau(t') G^*(y, t; y', t', c_{hy}, c_{th}) \|_{y=y'} dt', \quad (8)$$

where $G^*(y, t; y', t', c_{hy}, c_{th})$ is the kernel of the integral equation, which we present further in section 2.2 (see also Cole et al. (2010)). The kernel indicates the influence of the thermal load applied at position y' and time t' in the pore fluid pressure observed at position y and time t . Throughout our analysis we make the assumption that the maximum value of pore fluid pressure $P_{max}(t)$, at observation time (t) , lies at the point of application of the thermal load y' . This assumption is then verified numerically. Hence, the position of observation of $P_{max}(t)$, y , is equal to $y = y'$, and the kernel $G^*(y, t; y', t', c_{hy}, c_{th})$ needs to be calculated at $y = y'$.

We note that the frictional response is dependent on the strain localization mode and the boundary conditions applied at the fault gouge. The first influences the form of the thermal load as a function of time and position, while the latter influences the form of the kernel of the coupled linear thermo-hydraulic problem at hand. For the purposes of our analyses we will consider the cases of: 1) an unbounded fault gouge under a) a stationary PSZ, described in Rice (2006a), b) a traveling PSZ at a constant velocity v , and 2) a bounded fault gouge under a) a stationary PSZ, and b) a traveling PSZ, where position is a periodic function of time i.e. $y' = u(t')$ (see equation (2) and section 4). The periodic movement of the PSZ is justified on the basis of the numerical analyses presented previously in Part I (see Stathas and Stefanou (2022), Figures ??,??.) We present the relevant Green's function kernels in section 2.2. In order to solve the modified resulting Volterra integral equation (8), we have employed the collocation quadrature method described in Tang et al. (2008) as explained in section 3.

Having defined the differences between the classical and the extended model of thermal pressurization described in this section, we comment further on the differences between our linear extended model and the one used in the fully nonlinear analyses of Part I, Stathas and Stefanou (2022). In particular, in Part I, a micromorphic model together with THM couplings, was used for the determination of the PSZ thickness during coseismic slip. The application of a micromorphic continuum leads to a finite thickness for the PSZ, which guarantees mesh objectivity of the numerical results. Because the thickness of the

PSZ is finite, the thermal load applied inside the PSZ is distributed over the PSZ thickness. Furthermore, the finite thickness of the PSZ is a crucial part of the mechanism explaining the appearance of traveling PSZ inside the fault gouge as we have argued in Part I. We further note that the yield criterion employed in the analyses of Part I was a Drucker-Prager yield criterion, while, here we make use of a Mohr-Coulomb yield criterion. The use of the Mohr Coulomb criterion allows us to describe the friction $\tau(t)$ with the help of the normal stress σ_n to the yielding plane, instead of the combination of normal stresses required in the case of the Drucker-Prager.

2.2. Cases of Interest

We consider four cases for the loading and boundary conditions concerning the evaluation of the fault friction during coseismic slip. We first separate between stationary and traveling modes of strain localization and then we further discriminate between unbounded and bounded domains in order to cover all possible cases. The separation of the fault's frictional response into these categories leads to four different expressions for the Green's function kernel $G^*(y, t; y', t', c_{hy}, c_{th})$ in equation (8).

Here we will provide the analytical expressions, for the kernels to be substituted into equations (8). In naming the Green's function kernels we used the subscript naming conventions of Cole et al. (2010). Namely for diffusion in 1D line segment domains, the letter $X_{\alpha\beta}$ is adopted, where α, β are the left ($y = 0$) and right ($y = H$) boundaries of the domain respectively. They can take the values 0 or 1 indicating an unbounded or a bounded domain respectively, under homogeneous Dirichlet boundary conditions.

We begin by introducing the Green's function kernels of the unbounded X_{00} and the bounded X_{11} cases in the case of a 1D diffusion equation under homogeneous Dirichlet boundary conditions.

For the unbounded case we use:

$$G_{X_{00}}(y, t; y', t', c) = \frac{1}{2\sqrt{\pi c(t-t')}} \exp\left[-\frac{(y-y')^2}{4c(t-t')}\right]. \quad (9)$$

Similarly for the bounded case we use:

$$G_{X_{11}}(y, t; y', t', c) = \frac{2}{L} \sum_{m=1}^{\infty} \exp\left[-m^2 \pi^2 c \frac{t-t'}{H^2}\right] \sin\left(m\pi \frac{y}{H}\right) \sin\left(m\pi \frac{y'}{H}\right). \quad (10)$$

We note here that c can be either c_{th} or c_{hy} depending on the diffusion problem in question. The kernels $G_{X_{\alpha\beta}}^*(y, y', t-t', c_{hy}, c_{th})$ of the pressure diffusion problem based on the impulse of the frictional response for given boundary strain localization modes and boundary conditions are given by:

- Stationary mode of strain localization

- Unbounded domain, $\alpha = 0, \beta = 0, x' = 0$, (see Rice, 2006a)

$$G_{X_{00}}^*(y, t; 0, t', c_{hy}, c_{th}) = c_{hy} G_{X_{00}}(y, t; 0, t', c_{hy}) - c_{th} G_{X_{00}}(y, t; 0, t', c_{th}). \quad (11)$$

- Bounded domain $\alpha = 1, \beta = 1, x' = 0$

$$G_{X_{11}}^*(y, t; 0, t', c_{hy}, c_{th}) = c_{hy} G_{X_{11}}(y, t; 0, t', c_{hy}) - c_{th} G_{X_{11}}(y, t; 0, t', c_{th}). \quad (12)$$

- Traveling mode of strain localization

- Unbounded domain, $\alpha = 0, \beta = 0, y' = u(t')$:

$$G_{X_{00}}^*(y, t; y', t', c_{hy}, c_{th}) = c_{hy} G_{X_{00}}(y, t; u(t'), t', c_{hy}) - c_{th} G_{X_{00}}(y, t; u(t'), t', c_{th}). \quad (13)$$

- Bounded domain, periodic trajectory in time, $\alpha = 1, \beta = 1, y' = u(t')$:

$$G_{X_{11}}^*(y, t; y', t', c_{hy}, c_{th}) = c_{hy} G_{X_{11}}(y, t; u(t'), t', c_{hy}) - c_{th} G_{X_{11}}(y, t; u(t'), t', c_{th}). \quad (14)$$

3. Methods for the numerical solution of linear Volterra integral equations of the second kind

The solution of linear integral equations of the second kind can be sought with a variety of different analytical and numerical methods. From an analytical standpoint, these methods include methods from operational calculus namely, Laplace, Fourier or \mathcal{Z} -Transform (see Churchill, 1972; Brown et al., 2009; Mavaleix-Marchessoux et al., 2020), the use of Taylor expansions for the integrand inside the integral and the method of Adomian decomposition (see Wazwaz, 2011; Evans et al., 1981). The case of a stationary yielding mathematical plane described in Rice (2006a) can, and has been solved analytically, making use of the Laplace transform. Those methods depend on the convolution property of the integral in the integral equation to transform it into a simpler algebraic equation. The challenge then lies in the inversion of the relation obtained in the auxiliary (frequency) domain back to the time domain. However, as the complexity of the Green's function kernels and the loading function increases due to the introduction of boundary conditions and different assumptions concerning the trajectory of the shear band along the fault gouge, such an inversion is not always possible analytically. We are then forced to use numerical methods for the solution of the above Volterra integral equation.

The above analytical methods have also their numerical counterparts, with the use of the Discrete Fourier Transform (DFT) being a central part in most numerical solution procedures. However, use of the DFT is most efficient when the integral equation to be solved has the form of a convolution. This is not always the case in our problem. For instance, the kernel described in equation (14) has terms in (t, t') that do not involve their difference $(t - t')$, and therefore, its use in equation (8) results in the integral term not being a convolution. In order to handle the above difficulty then, we will make use of another class of numerical methods called spectral collocation methods, which solve the integral equation (8) directly in the time domain. These methods are conceptually easy to use, and since no inversion is required, they are able to handle very general cases of Green's function kernels and loading functions.

In what follows, we will make use of the Spectral Collocation Method with Lagrange basis functions (SCML) for the numerical solution of the integral equation (8) (see Tang et al., 2008; Elnagar and Kazemi, 1996, and section 3.1). The SCML method will be shown to handle both the bounded and unbounded domains and the cases of stationary vs traveling strain localization.

3.1. Collocation method

We begin by normalizing equation 8. We choose the following normalization parameters $t_0 = \frac{H^2}{c_{th}}$, $\tau_0 = f(\sigma_n - p_0)$, $y_0 = H$, $r_c = \frac{c_{hy}}{c_{th}}$. The normalized equation is the given by:

$$\bar{\tau}(\bar{t}) = 1 - \frac{f\Delta V}{\rho C} \frac{H}{c_{th}(r_c - 1)} \int_0^{\bar{t}} \bar{\tau}(\bar{t}') \bar{G}^*(\bar{y}, \bar{t}; \bar{y}', \bar{t}') \big|_{y=y'} d\bar{t}' \quad (15)$$

where $\bar{\tau} = \frac{\tau}{\tau_0}$, $\bar{t} = \frac{t}{t_0}$, $\bar{t}' = \frac{t'}{t_0}$, $\bar{y} = \frac{y}{y_0}$, $\bar{y}' = \frac{y'}{y_0}$ and $\bar{G}^*(\bar{y}, \bar{t}; \bar{y}', \bar{t}')$ is the normalized Green's function kernel given by:

- In the unbounded case:

$$\bar{G}_{X00}^*(\bar{y}, \bar{t}; \bar{y}', \bar{t}') = \frac{1}{2} \left[\frac{r_c}{\sqrt{\pi r_c(\bar{t} - \bar{t}')}} \exp \left[-\frac{(y - y')^2}{4r_c(\bar{t} - \bar{t}')} \right] - \frac{1}{\sqrt{\pi(\bar{t} - \bar{t}')}} \exp \left[-\frac{(y - y')^2}{4(\bar{t} - \bar{t}')} \right] \right] \quad (16)$$

- In the bounded case:

$$\bar{G}_{X11}^*(\bar{y}, \bar{t}; \bar{y}', \bar{t}') = 2 \left[r_c \sum_{m=1}^{\infty} \exp \left[-(m\pi)^2 r_c (\bar{t} - \bar{t}') \right] - \sum_{m=1}^{\infty} \left[-(m\pi)^2 r_c (\bar{t} - \bar{t}') \right] \right] \sin(m\pi \bar{y}) \sin(m\pi \bar{y}') \quad (17)$$

Based on the work of Tang et al. (2008), we apply a spectral collocation method for the calculation of the frictional response described by equation (15). Spectral methods allow for evaluation of the solution in the whole domain of the problem yielding exponential degree of convergence (see Tang et al. (2008)). The principle of the method is the substitution of the unknown function $\bar{\tau}(\bar{t})$ inside the integral equation by a series of polynomials that constitute a polynomial basis. We then opt for the minimization of

the residual between the exact and the approximate solution at specific collocation points inside the problem's domain. Here we use the Chebyshev orthogonal polynomials of the first kind (see Trefethen (2019)). Because the Chebyshev polynomial of the first kind constitute a basis in the interval $[-1,1]$, we transform the integral equation (15) to lie in this interval (see Appendix Appendix C). The integral equation then reads:

$$U(\bar{z}) = 1 - \frac{f\Lambda V}{\rho C} \frac{H}{c_{th}(r_c - 1)} \frac{\bar{T}}{2} \int_{-1}^{\bar{z}} U(s) G^* \left(\bar{y}, \frac{\bar{T}}{2}(\bar{z} + 1); \bar{y}', \frac{\bar{T}}{2}(s + 1) \right) ds, \quad (18)$$

where we note that $U(\bar{z}) = \bar{\tau}(\frac{\bar{T}}{2}(\bar{z} + 1))$. In the previous equation we performed a change in the integration variable from $\bar{t} \in [0, \frac{\bar{T}}{2}(\bar{z} + 1)]$ to $s \in [-1, \bar{z}]$ so that the unknown function $U(s)$ inside the integral remains in the same form as $U(\bar{z})$ outside the integral. Next, we choose to approximate the unknown function in equation (18) (i.e. frictional response) by its Lagrange interpolation i.e:

$$U(\sigma) \approx \sum_{j=0}^N U(\bar{z}_j) F_j(\sigma) \quad (19)$$

The Lagrange interpolation allows a function to be approximated as a linear combination of the Lagrange cardinal polynomials $F_j(\sigma)$, and weights $U(\bar{z}_j)$ corresponding to the values of the function at specific points \bar{z}_j . The Lagrange cardinal polynomials have the property that $F_m(\bar{z}_n) = \delta_{mn}$, where δ_{mn} is the kronecker symbol. We choose to express the Lagrange polynomials with the help of the Chebyshev polynomials of the first kind, and we choose the set of approximation nodes \bar{z}_j to correspond to the extrema of the Chebyshev polynomial of the first kind, of degree N (see Trefethen (2019)). In this case the interpolating polynomial is written as follows:

$$U(\sigma) \approx \sum_{j=0}^N U(\bar{z}_j) P_j(\sigma), \quad (20)$$

$$P_j(\sigma) = \begin{cases} \frac{(-1)^j}{\sigma - \bar{z}_j} / \sum_{k=0}^N \frac{(-1)^k}{\sigma - \bar{z}_k} & \sigma \neq \bar{z}_j \text{ or } \sigma \neq \bar{z}_k \\ 2 & \sigma = \bar{z}_0 \text{ or } \sigma = \bar{z}_N \\ 1 & \sigma = \bar{z}_j \text{ and } j \neq 0 \text{ or } j \neq N \\ 0 & \sigma = \bar{z}_k \end{cases} \quad (21)$$

$$\sum_{j=0}^N U(\bar{z}_j) = \sum_{j=0}^N U(\bar{z}_j) - \frac{U(\bar{z}_0) + U(\bar{z}_N)}{2} \quad (22)$$

where the barycentric formula involving the modified sum $\sum_{j=0}^N U(\bar{z}_j)$ is used for the cardinal polynomials and the interpolation (see Trefethen (2019)). By making use of the barycentric formula in equation (21) we are able to evaluate the cardinal polynomials fast and with smaller error than other conventional approaches (see Trefethen (2019); Tang et al. (2008)). We note that the Lagrange interpolation polynomial at the selection of Chebyshev points $\{\bar{z}_i\}$ stays unaffected by Runge's phenomenon. Runge's phenomenon is the observation that the high polynomial degree Lagrangian interpolation in equidistant grids leads to high error at the approximation of points that don't belong to the set of interpolation nodes. The effect is more pronounced near the boundaries of the interpolation domain.

For the numerical evaluation of the integral in equation (18) the Clenshaw-Curtis quadrature will be used since it is compatible with the interpolation nodes used. We note here that the choice of the interpolation nodes \bar{z}_j -extrema of the degree N Chebyshev polynomial of first kind- leads to quadrature weights of positive sign, which reduces the error of the summation. If equidistant points were used as a quadrature rule of high order ($N > 7$), this would lead to quadrature weights of alternating sign increasing the integration error Quarteroni et al. (2007). We transform once again the integral of equation (18) from $s \in [-1, \bar{z}]$ to $\theta \in [-1, 1]$ in order to apply the appropriate quadrature rule for integration. the new integral equation reads:

$$U(\bar{z}) = 1 - \frac{f\Lambda V}{\rho C} \frac{H^2}{c_{th}(r_c - 1)} \frac{\bar{T}}{2} \frac{\bar{z} + 1}{2} \int_{-1}^1 U(s(\bar{z}, \theta)) G^* \left(\bar{y}, \frac{\bar{T}}{2}(\bar{z} + 1); \bar{y}', \frac{\bar{T}}{2}(s(\bar{z}, \theta) + 1) \right) ds, \quad (23)$$

The discretized form of equation (23) for the Clenshaw Curtis quadrature scheme is given by:

$$U(\bar{z}_i) = 1 - a \bar{t}_i \sum_{j=0}^N U_j(\bar{z}_j) \sum_{p=0}^N P_j(s_{ip}) G^* (\bar{y}, \bar{t}_i; \bar{y}', \bar{t}'_{ip}) w_p, \quad (24)$$

where, $s_{ip} = s(\bar{z}_i, \theta_p)$, $\bar{t}_i = \frac{\bar{z}_i + 1}{2} \bar{T}$, $\bar{t}'_{ip} = \frac{\bar{T}}{2} (s_{ip} + 1)$, $a = \frac{f \Delta V}{\rho C} \frac{H^2}{c_{th}(r_c - 1)} \frac{\bar{T}}{2}$.

Finally, by adopting the indicial notation with summation over repeated indices our system is written as:

$$(\delta_{i,j} + A_{i,j}^*) U_j(\bar{z}_j) = g_i, \quad (25)$$

where $g_i = 1$ and $A_{i,j}^*$ is given by:

$$A_{i,j}^* = A_{ij} - B_{ij} \quad (26)$$

$$A_{ij} = a \bar{t}_i \sum_{p=0}^N P_j(s_{ip}) G^* (\bar{y}, \bar{t}_i; \bar{y}', \bar{t}'_{ip}) w_p \quad (27)$$

$$B_{ij} = \begin{cases} A_{i0} & , j = 0 \\ A_{iN} & , j = N \\ A_{ij} & , j \neq 0 \text{ or } j \neq N \end{cases} \quad (28)$$

or in matrix form:

$$(I + A^*) U = G, \quad (29)$$

We can then solve the algebraic system to find the interpolation coefficients U_j of the numerical solution. Due to the properties of the Lagrange polynomials the coefficients U_i are also the values of the numerical solution at the specific times t_i .

4. Applications

In this section we will present the evolution of the frictional strength $\tau(t)$ for the different cases of loading and boundary conditions described in section 2.2. The available values for the fault gouge properties considered homogeneous along its height are given in Table 1.

Parameters	Values	Properties	Parameters	Values	Properties
f	0.5	-	Λ	2.216	MPa/ $^{\circ}\text{C}$
σ_n	200	MPa	ρC	2.8	MPa/ $^{\circ}\text{C}$
P_0	66.67	MPa	c_{hy}	10	mm ² /s
H	1	mm	c_{th}	1	mm ² /s

Table 1: Material parameters of a mature fault at the seismogenic depth (see Rice, 2006b; Rattez et al., 2018).

4.1. Stationary strain localization mode

4.1.1. Stationary strain localization on an unbounded domain

The solutions for the temperature field on an infinite layer under a stationary point source thermal load were first derived in Carslaw and Jaeger (1959). Mase and Smith (1987) and Andrews (2005), present temperature field solutions for stationary distributed thermal loads. Later in Lee and Delaney (1987) the authors used the above temperature solutions to derive the pressure solution fields $\Delta P(y, t)$ of the coupled pore fluid pressure equation.

In the work of Rice (2006a); Rempel and Rice (2006) the authors introduce a methodology for the determination of the coupled frictional response of a fault gouge under constant shear rate. The results for the stationary instability on an infinite domain have already been derived in Rice (2006b) for yielding on a mathematical plane, and further expanded in the case of distributed yield in Rempel and Rice

(2006). In this case, a closed form analytical solution is possible: $\tau(\delta) = f(\sigma_n - p_0) \exp(\frac{\delta}{L^*}) \operatorname{erfc}(\sqrt{\frac{\delta}{L^*}})$, where $L^* = \frac{4}{f^2} \left(\frac{\rho C}{\Lambda} \right)^2 \frac{(\sqrt{c_{hy}} + \sqrt{c_{th}})^2}{\dot{\delta}}$. The derived solution is recognized as the Hermite polynomial of degree -1.

We note that this solution is dependent on the seismic slip rate $\dot{\delta}$ (see dimensions of L^*). The dependence of the fault friction on the seismic slip rate $\dot{\delta}$ (velocity weakening) has been shown in experiments (see Badt et al., 2020; Harbord et al., 2021; Rempe et al., 2020, among many others). In order to demonstrate the efficiency of the SCLM method, we use the above analytical solution as a benchmark for comparison. In Figure 3 we present the numerical results of slip on a stationary mathematical plane.

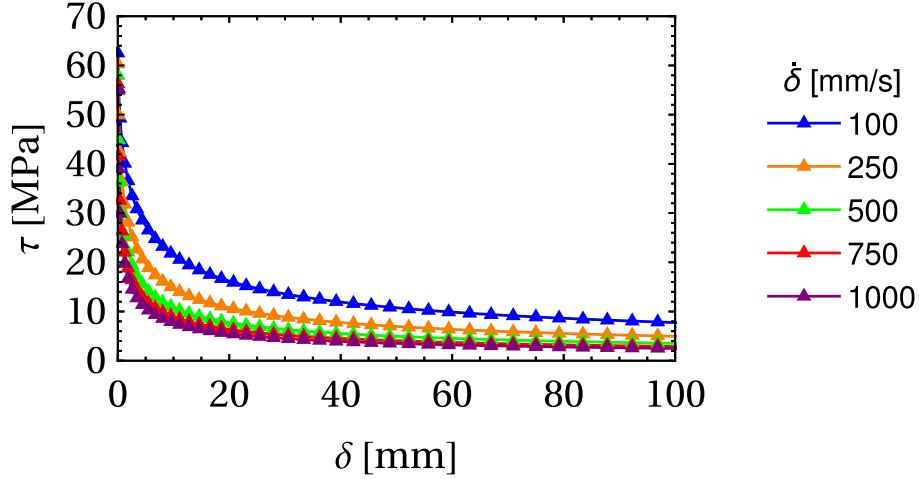


Figure 3: Left: $\tau - \delta$ response of the layer for different slip velocities $\dot{\delta}$ applied. Due to the constant isothermal drained conditions at the boundary near infinity the solution tends asymptotically to the zero steady state solution. For different values of the velocity $\dot{\delta}$, the analytical solution is presented by a continuous line and the numerical solution is presented by the triangle markers. The numerical solution obtained by the SCLM method, coincides to the analytical curves.

To showcase further the accuracy of our results, we present the calculated temperature $\Delta T(y, t)$ and pressure $\Delta P(y, t)$ fields, computed with the method of Gaussian quadrature at the already computed Chebyshev nodes for the time domain, in a uniform spatial grid around the position of strain localization. The results of Figure 4 indicate that at all times the pressure maximum coincides with the position of the strain localization as expected from the analytical solution. This corroborates the accuracy and precision of our results.

4.1.2. Stationary strain localization on a bounded domain

When the yielding region (PSZ) is wholly contained on a mathematical plane one might assume that the true boundaries of the fault gouge play little role in the evolution of the phenomenon, simulating the fault gouge region as an infinite layer. However, the validity of this model depends heavily on the pressure and temperature diffusion characteristic times in comparison to the total evolution time of the seismic slip. In essence, the question is: Does the phenomenon evolve so fast that the boundaries do not play a role in the overall frictional response?

This is a valid question, considering that in experiments and in the majority of the numerical simulations, we need to assign some kind of boundary conditions to the problem in question. We address this question by investigating the case of a stationary strain localization (point thermal source) in the middle of a bounded domain representing the fault gouge, with the linear Volterra integral equation of the second kind (15). We do so by applying the new form of the kernel $G_{X11}^*(x, x', t - t', c_{hy}, c_{th})$, which takes into account the boundary conditions of coseismic slip, pressure and temperature discussed in Part I, Stathas and Stefanou (2022). Namely, the domain of the fault gouge was assumed to have a width of $H = 1$ mm. We remind also that the boundary conditions correspond to an isothermal ($\Delta T(0, t) = \Delta T(H, t) = 0$) drained ($\Delta P(0, t) = \Delta P(H, t) = 0$) case.

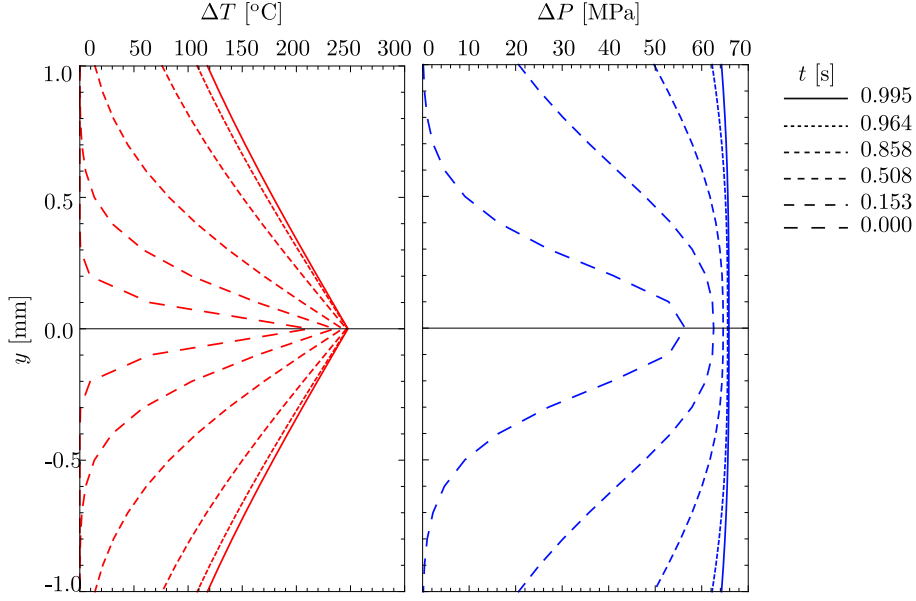


Figure 4: Temperature ΔT and pore fluid pressure ΔP fields along the height of the layer for shearing velocity $\dot{\delta} = 1$ m/s, at different times during the analysis. The numerical solution is consistent with the analytical observation that the position of ΔP_{max} coincides with the position of the stationary strain localization.

In order to solve equation (15) for the new kind of boundary conditions, we need to derive the new expressions for the Green's function kernel for the thermal diffusion and coupled pore fluid pressure diffusion equations on the bounded domain. The expression for the bounded Green's function kernel under Dirichlet boundary of the heat diffusion equation (17), can be found by applying the method of separation of variables according to Cole et al. (2010).

Equation (17) is termed the long co-time Green's function kernel. A mathematically equivalent short co-time solution can be constructed making use of the Green's kernel defined for the infinite domain case via the method of images, however, its form is significantly more complicated than equation (17) and is not convenient for the numerical procedures used in this paper. Namely, the short co-time solution is best suited when studying transient diffusion at the very start of the phenomenon. For fast timescales we don't need a lot of terms for the short co-time series to converge to the expected degree of accuracy. However, for large timescales after the initiation of the phenomenon the large co-time solution converges faster, i.e. using fewer terms in the sum. Furthermore, the form of the large co-time solution has a simpler form and can be integrated numerically faster, i.e. with less machine operations, than that of the short co-time.

Next, we need to obtain the Green's function for the coupled pore fluid pressure diffusion equation. This is done by solving the coupled pressure differential equation on the bounded domain, using the method of separation of variables. We note that the two diffusion problems (thermal and coupled pore fluid pressure) are bounded by Dirichlet boundary conditions on the same domain and therefore, their Fourier expansions belong to the same Sturm-Liouville problem. This allows us to express, for the first time in the literature, the Green's function kernel of the coupled temperature diffusion system on a bounded domain due to an impulsive thermal load. Full derivation details are shown in Appendix B, where we prove that the kernel in question can be given in a manner similar to the original expression for the infinite domain case found in Lee and Delaney (1987).

Next, we apply the kernel of equation (17) in the equation (15). Using the SCLM method, the values of friction at specific values of time (t) and seismic slip displacement (δ) can be derived for different seismic slip velocities ($\dot{\delta}$). The results of such an analysis are presented in Figure 5.

We note here that contrary to the results obtained in the case of the infinite layer in Rice (2006a); Rempel and Rice (2006), where the frictional response is decreasing monotonously (see also Figures 3,4), in the case of the stationary thermal load on a bounded layer the frictional response is eventually influenced by the boundaries of the domain (see Figures 6,7). Since the conditions on the boundaries are constant in time and the frictional source provides heat to the layer at a rate that is bounded by a constant

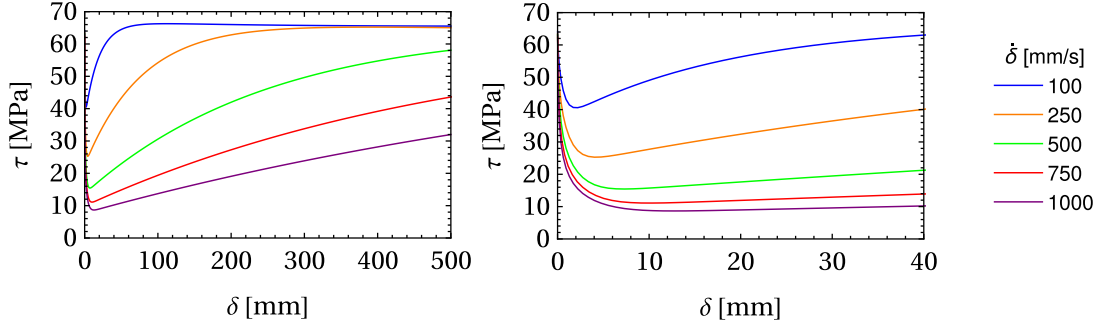


Figure 5: $\tau - \delta$ response of the layer for different slip velocities $\dot{\delta}$ applied. We observe that as the shearing rate increases, the softening behavior becomes more pronounced. For typical values of the seismic slip displacement we note that the effect of the boundaries becomes important. Due to the existence of a steady state the fault recovers all of its strength lost due to thermal pressurization at the beginning of the coseismic slip.

($\frac{1}{\rho C} \tau(t) \dot{\delta} \leq \frac{1}{\rho C} \tau_0 \dot{\delta} = M$), the temperature field will eventually reach a steady state. This in turn means that at the later stages of the phenomenon the temperature profile will remain constant in time, therefore its rate of change $\frac{\partial \Delta T}{\partial t}$ will become zero. Consequently, the phenomenon of thermal pressurization will cease, leading to rapid pore fluid pressure decrease due to the diffusion at the boundaries. As a result pore fluid pressure will return to its ambient value, and therefore, friction will regain its initial value too.

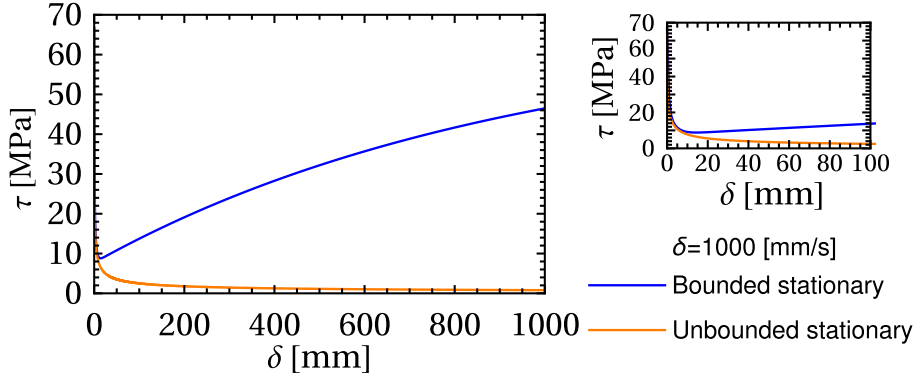


Figure 6: Comparison of the $\tau - \delta$ response of the layer for an applied slip velocity $\dot{\delta} = 1000$ mm/s. We observe that the influence of the boundaries becomes important from the early stages of coseismic slip ($\delta \approx 10$ mm). In the bounded case, due to the existence of a steady state the fault tends to recover all of its strength lost to thermal pressurization at the beginning of the phenomenon. namely for a typical value of coseismic slip $\delta = 1000$ mm, the fault has recovered more than half of its initial frictional strength.

It is important to note here that as we show in Figure 6, frictional regain happens well inside the time and coseismic slip margins observed in nature during evolution of the earthquake phenomenon. Of course frictional regain depends on the height of the layer. Namely as the height of the layer increases, the stress drop due to thermal pressurization at the initial stages becomes larger and the fault gouge recovers its frictional strength slower and in later stages of slip. However, the height of the fault gouge $H=1$ mm corresponds to typical values from fault observations around the globe (see Myers and Aydin, 2004; Rice, 2006a; Sibson, 2003; Sulem et al., 2004, among others). Furthermore, based on the significantly higher hydraulic, and to a lesser extent thermal, diffusivities of the surrounding damaged zone (see Part I Aydin, 2000; Tanaka et al., 2007), we conclude that the assumption of isothermal drained conditions at the boundaries of the fault gouge as a first approximation, is also justified. We note in particular that for a mature fault gouge, the ratio of the hydraulic permeability and thermal conductivity of the fault gouge (f) to the surrounding damaged zone (d) lies between $r_{hy} = \frac{k_{hy}^f}{k_{hy}^d} = 10^2 \sim 10^6$, $r_{th} = \frac{c_{th}^f}{c_{th}^d} = 1 \sim 10$. Therefore, the a priori assumption that an infinite layer describes adequately well the fault gouge during seismic slip should, in our opinion, be revised.

Next, we provide in Figure 7 the field numerical solutions for the change in temperature and pressure in a bounded domain of height $H = 1$ mm, under constant seismic slip rate $\dot{\delta} = 1$ m/s. In the bounded domain, the fields of temperature and pressure will reach the steady state, while the maximum

pore fluid pressure coincides with the position of the stationary strain localization. However the steady state reached now is one where full frictional regain takes place. Therefore, the predicted temperature field at the steady state is not applicable, since other weakening mechanisms will take place (e.g. thermal decomposition of minerals will start at 900 °C, see Sulem and Famin (2009); Sulem and Stefanou (2016)). The role of the boundary conditions at the fault gouge level becomes very important.

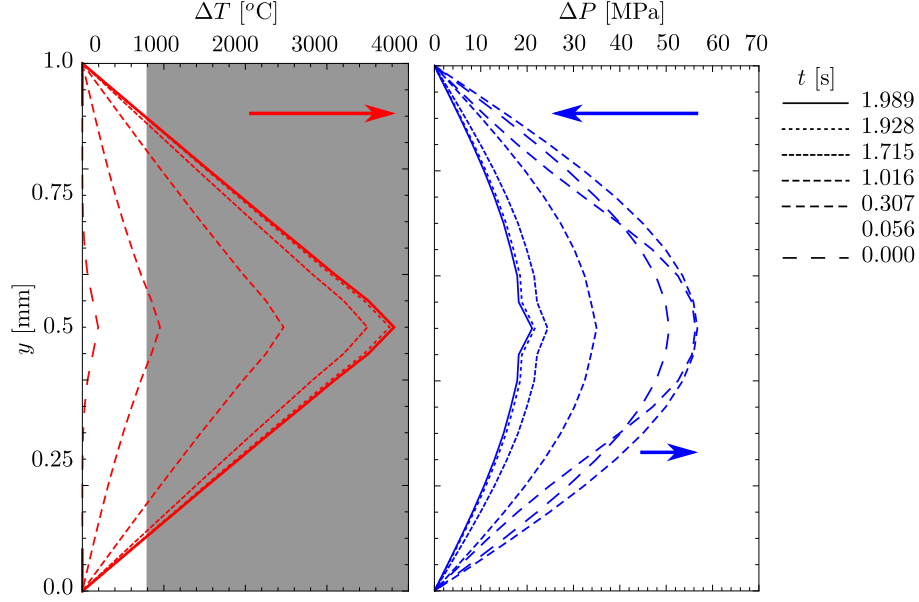


Figure 7: Temperature ΔT and pore fluid pressure ΔP fields along the height of the layer for shearing velocity $\dot{\delta} = 1$ m/s, at different times during the analysis. The numerical solution is consistent with the analytical observation that the position of ΔP_{max} coincides with the position of the stationary strain localization. The arrows indicate the evolution course of the maxima of each field. The pressure field initially increases before subsiding when the temperature field progressively reaches steady state and thermal pressurization ceases. The shaded area, indicates a range of temperatures ($\Delta T \geq 800^\circ\text{C}$), that is prohibitively large inside the fault gouge since it corresponds to melting of the gouge material. Moreover, at $\Delta T \geq 600^\circ\text{C}$ chemical decomposition of minerals will start to take place inside the gouge, antagonizing the weakening mechanism of thermal pressurization.

4.2. Traveling mode of strain localization

In the available literature Rice (2006a,b) and the subsequent works Rempel and Rice (2006); Platt et al. (2014b); Rice et al. (2014a) one of the main assumptions is that the principal slip zone (PSZ), which is described by the profile of the plastic strain rate (localized on a mathematical plane or distributed over a wider zone) remains stationed in the same place during shearing of the infinite layer. In this work we depart from this assumption, by assuming that the principal slip zone is traveling inside the fault gouge.

Two cases will be discussed, the first one discusses the implications of a traveling shear band inside the infinite layer, while the other case focuses on a moving shear band inside the bounded layer. The difference between a stationary and a moving shear band is that in the second case a steady state for the temperature $\Delta T(y, t)$ and pressure $\Delta P(y, t)$ fields is not possible (i.e. their rates of change cannot become zero, $\frac{\partial \Delta T}{\partial t} \neq 0$, $\frac{\partial \Delta P}{\partial t} \neq 0$), since the profile of temperature constantly changes due to the thermal load constantly moving around the domain. This ensures that thermal pressurization never ceases. Thus, the value of the residual friction τ_{res} depends on the fault gouge's thermal and hydraulic properties (c_{th} , c_{hy}), the coseismic slip velocity $\dot{\delta}$, and the traveling velocity of the strain localization mode (v). This has serious implications for the frictional response of the layer during shearing. More specifically, as the load does not stay stationary, thermal pressurization does not have enough time to act by increasing the pore fluid pressure. Therefore, according to the Mohr-Coulomb yield criterion, friction does not vanish as in the case of Rice (2006a). Instead friction reaches a residual value τ_{res} different than zero. This is central for the dissipated energy (see Andrews, 2005; Kanamori and Brodsky, 2004b; Kanamori and Rivera, 2006, among others) and the control of the fault transition from steady to unsteady seismic slip.

4.2.1. Traveling mode of strain localization in the unbounded domain.

Here we consider the shearing of a fault gouge, whose boundaries are taken at infinity. In what follows, we distinguish between the seismic slip velocity $\dot{\delta}$ and the velocity of the traveling shear band $v(t)$. In

Figure 8, we consider the PSZ (moving point heat source) to travel inside the fault gouge with a velocity $v=50$ mm/s. Different values for the rate of coseismic slip parameter $\dot{\delta}$ are taken into account. The shear band velocity v is in agreement with observations from the numerical results of Part I Stathas and Stefanou (2022). Contrary to the results obtained in the case of a stationary strain localization studied in Rice (2006a), our results indicate the existence of a lower bound in the frictional strength τ_{res} , dependent on the rate of seismic slip $\dot{\delta}$ (see Figure 9).

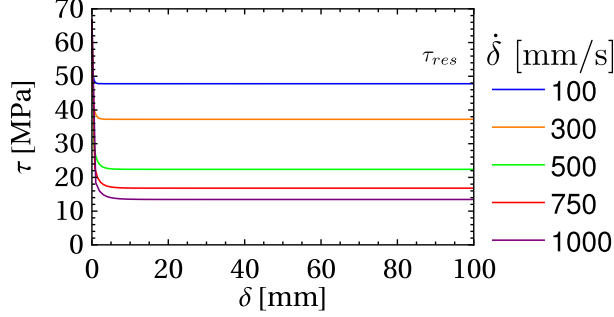


Figure 8: $\tau - \delta$ response of the layer for different slip velocities $\dot{\delta}$ applied. We observe that as the shearing rate increases, the softening behavior becomes more pronounced. Higher seismic slip rates correspond to lower residual values for friction.

In Figure 8, we observe that an increase in seismic slip velocity $\dot{\delta}$ leads to a decrease of the frictional plateau. Since the plateau reached in these cases is other than the initial friction value corresponding to the ambient pore fluid pressure, we conclude that thermal pressurization is still present in the model's response. This is true, since the profile of temperature changes continuously, due to the yielding plane moving at a constant velocity v . This forces the maximum temperature, T_{max} , to move in the same way. Thus, the rate of change of the temperature field $\frac{\partial \Delta T}{\partial t}$, which is the cause of thermal pressurization, does not vanish.

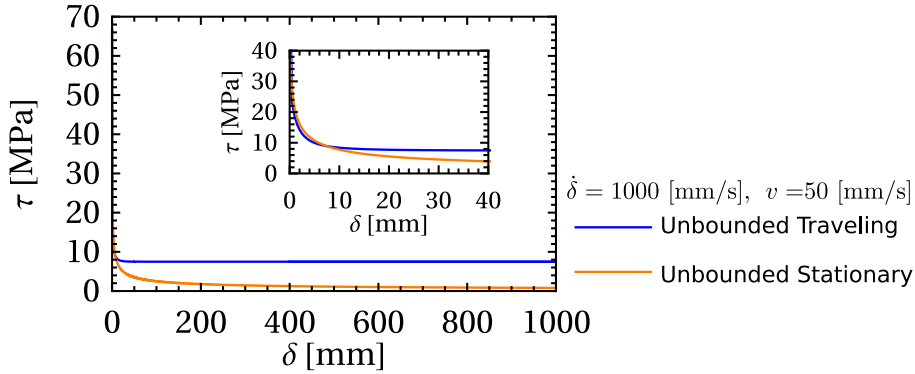


Figure 9: Comparison of the $\tau - \delta$ frictional response between a moving and a stationary strain localization (PSZ) in an unbounded domain. The assumption of a traveling strain localization leads to a plateau of non zero residual friction τ_{res} , contrary to the solution of Rice (2006a), which is based on a stationary PSZ.

In Figure 10, we plot the frictional response of the fault for a given seismic slip velocity $\dot{\delta} = 1$ m/s treating the shear band velocity v as a parameter. We notice that the slower moving shear bands force the fault to faster and larger frictional strength drops, before they eventually reach a plateau. This is consistent with the observations made in Rice (2006a), where the stationary shear band that presents an infinite negative slope at the start of the slip δ and tends asymptotically to zero as δ increases, can be treated as a special case of the model of traveling localization mode as the shear band velocity tends to zero ($v = 0$).

In Figure 11, we present the evolution with time of the temperature $\Delta T(y, t)$ and pressure increase $\Delta P(y, t)$ fields, in the region of the unbounded domain covered by traveling strain localization mode. We note that in this case the traveling localization mode leads to a distribution of the thermal load inside the domain, which -since thermal pressurization remains constant- leads to significantly lower values of

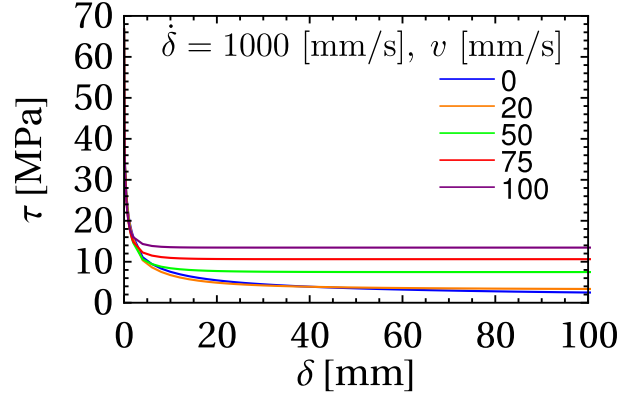


Figure 10: Frictional response $\tau - \delta$ of the layer for different velocities v of the traveling PSZ. For low traveling velocities the response tends to the behavior of stationary slip on a mathematical plane. As the traveling velocity increases the drop in friction becomes less.

temperature inside the domain. We note that the frictional response shown in Figure 8 is consistent with the pressure increase $\Delta P(y, t)$ inside the domain, while the temperature and pressure fronts coincide with the prescribed position of the traveling strain localization (thermal load).

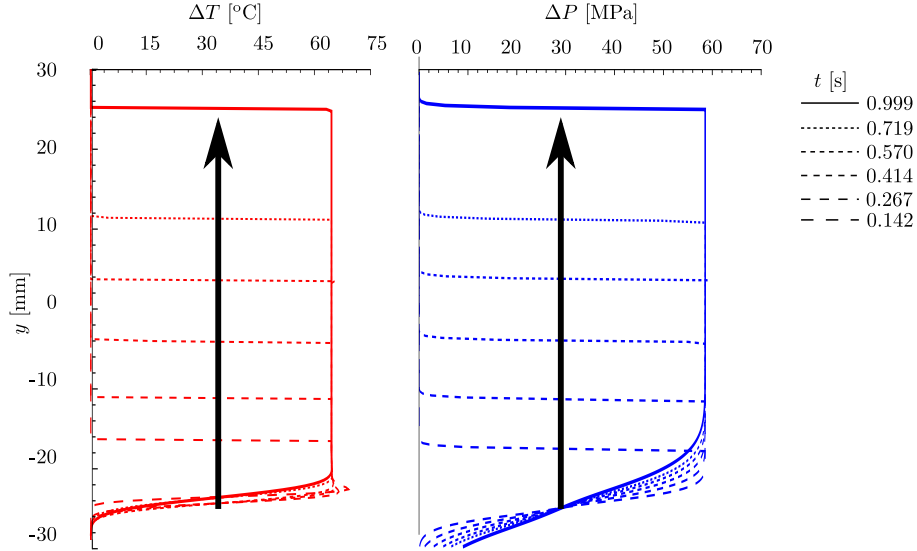


Figure 11: Temperature ΔT and pore fluid pressure ΔP fields along the height of the layer for shearing velocity $\dot{\delta} = 1$ m/s, at different times during the analysis. The numerical solution is consistent with the analytical observation that the position of ΔP_{max} coincides with the position of the stationary strain localization.

4.2.2. Traveling mode of strain localization in the bounded domain.

In this section we investigate the frictional response of the layer of height $H = 1$ mm, when the plastic strain localization (PSZ) travels inside a predefined region with a width $h = 0.6$ mm as shown in Figure 12. This region has the same width as the width of the plastified region predicted by our numerical model in Part I, Stathas and Stefanou (2022) see Figure ??). Based on the numerical results of Part I, we apply a periodic mode of traveling strain localization, with a constant velocity $v = 30$ mm/s. We prescribe the trajectory of the yielding plane, whose position $u(t)$ is given by a triangle pulse train:

$$u(t) = \frac{H}{2} + \frac{h}{2H} Tr(vt), \quad (30)$$

where H is the height of the layer, h is the width of the plastified region, v is the velocity of the strain localization and $Tr(\cdot)$ is the triangle wave periodic function. The period is given by $T = \frac{2h}{v}$. The resulting linear Volterra integral equations of the second kind is solved numerically by making use of the spectral collocation method in section 3.

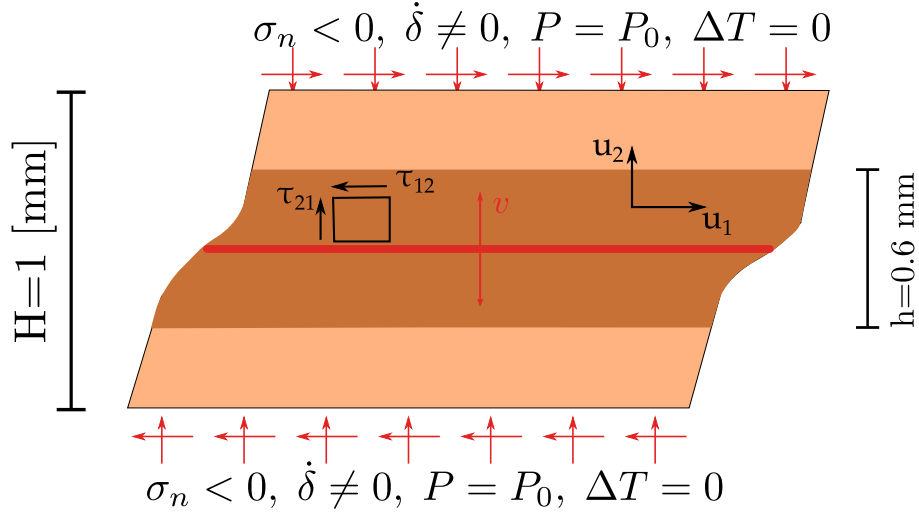


Figure 12: Schematic representation of a fault gouge of height $H = 1$ mm, under seismic slip δ . The PSZ - red line- is allowed to travel in a region of thickness $h=0.6$ mm according to the numerical results of Part I, Stathas and Stefanou (2022). The PSZ is moving periodically inside the region h with velocity v .

We observe in Figure 13 that as the shearing rate increases, the softening behavior becomes more pronounced. For typical values of the seismic slip displacement we note that the effect of the boundaries becomes important. The frictional response presents oscillations due to the periodic movement of the strain localization. Since the strain localization is constantly moving, a steady state is not possible for the fields of temperature and pressure ($\frac{\partial \Delta T}{\partial t} \neq 0 \rightarrow \frac{\partial \Delta P}{\partial t} \neq 0$). This means that the friction presents a residual value, τ_{res} , which is lower than the fully recovered value of the stationary bounded case.

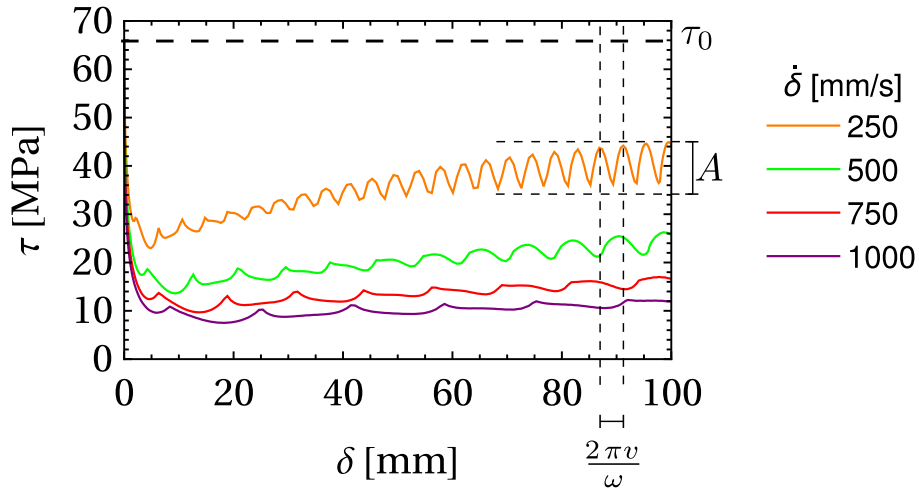


Figure 13: $\tau - \delta$ response of the bounded layer for different slip velocities $\dot{\delta}$ applied. A periodic traveling localization mode is applied. We observe that as the shearing rate increases, the softening behavior becomes more pronounced. For typical values of the seismic slip displacement we note that the effect of the boundaries becomes important. As the periodic traveling localization mode is constantly moving, a steady state is not possible. This means that the friction presents an oscillating residual value lower than the fully recovered value of the stationary bounded case.

Assuming the material parameters c_{th}, c_{hy} and the height of the layer H constant, characteristics such as the oscillations amplitude A , circular frequency ω and the residual value of friction τ_{res} are controlled by three parameters, the thickness of the prescribed region the PSZ is allowed to travel inside the layer, h , the velocity of the traveling PSZ, v , and the seismic slip rate applied at the fault gouge, $\dot{\delta}$.

In Figure 14, we investigate the influence of the shearing velocity $\dot{\delta}$, the velocity of the traveling shear band v on the frictional response of a fault gouge with height $H = 1$ mm. We note that the period of oscillations in the frictional response depends on the velocity with which the shear band travels inside the fault gouge. For the range of applied traveling shear band velocities 30 – 50 mm/s the minima and

maxima of the frictional response $\tau - \delta$ are not affected.

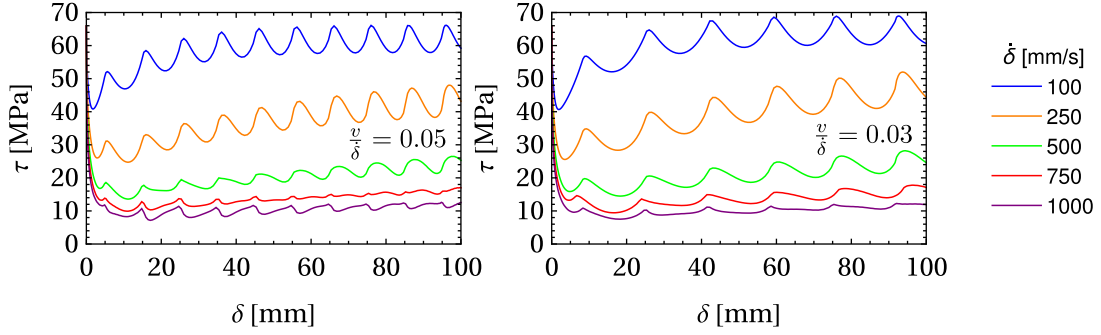


Figure 14: $\tau - \delta$ response of the bounded layer for different ratios of strain localization velocities v to coseismic slip rates $\dot{\delta}$ applied ($\frac{z}{\delta}$). We note that for the same rate the period of oscillation remains the same. The period of oscillations is depends on the height of the layer H and the velocity of the strain localization.

In Figure 15, we present a comparison between the friction developed during shearing of a bounded fault gouge and the model of slip on a stationary mathematical plane presented in section 4.1.1 and in Rice (2006a). In the bounded fault gouge, the seismic slip velocity is given by $\dot{\delta} = 1000$ mm/s. We further consider the shear band to travel with a velocity $v = 30$ mm/s inside a predefined region of height $h = 0.6$ mm. We note that the two responses differ. The periodic movement of the yielding plane (thermal load) inside the layer leads to frictional oscillations. This happens because the yielding plane moves towards the isothermal drained boundaries that function as heat and pressure sinks. Namely, the crests of the oscillations correspond to the time instance the load approaches the fault gouge boundaries, while troughs correspond to the time the PSZ is closer to the middle of the layer. We note here that the average friction inside the layer, τ_{ave} , is increasing due to the diffusion of pressure and temperature at the boundaries of the fault gouge. We note also that the oscillatory movement of the fault gouge moves excess heat and pressure towards the boundaries of the fault gouge leading to a ventilation phenomenon that further enhances the recovery of frictional strength. It is likely that removing the invariance along the slip direction would lead to vortices and other convective phenomena inside the layer (see Griffani et al., 2013; Miller et al., 2013; Rognon et al., 2015). However, 2D and 3D phenomena inside the fault gouge are not explored here.

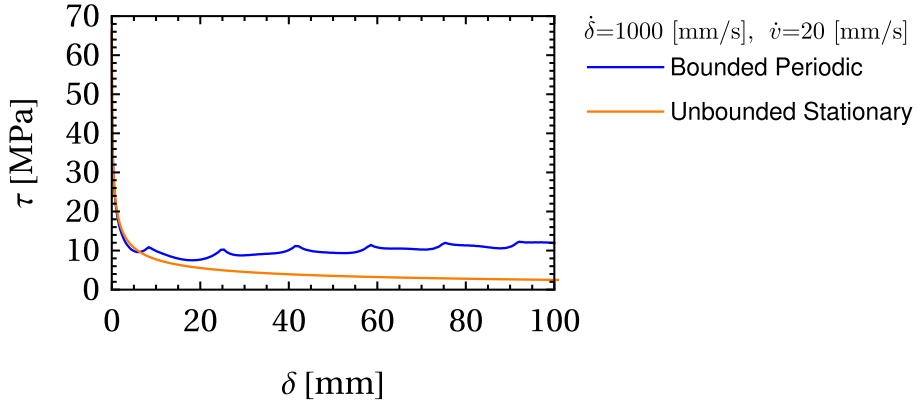


Figure 15: Comparison of the $\tau - \delta$ frictional response between a moving periodic strain localization on a bounded domain and a stationary strain localization (PSZ) on an unbounded domain. The influence of the boundary conditions is noticeable from the initial stages of the coseismic slip ($\delta \approx 10$ mm).

The results obtained in Figures 13,14, 15, present a qualitative agreement with those of Part I Stathas and Stefanou (2022). The difference in the values is due to the assumption of a Dirac load in this paper, in order to preserve the equilibrium inside the band. Assuming a distribution of the yielding rate $\dot{\gamma}^p$ that is not singular while respecting the equilibrium conditions along the layer -as it is the case for the Cosserat continuum- would allow for higher minima in the frictional response, because of the distributed thermal load over the finite thickness of the yielding region. This leads to more efficient diffusion at the initial stages of thermal pressurization.

In Figure 16 we present the fields of temperature $\Delta T(y, t)$ and pore fluid pressure increase $\Delta P(y, t)$ during shearing of the bounded fault gouge, with coseismic slip rate $\dot{\delta} = 1$ m/s, assuming a traveling mode of strain localization traveling with a velocity of $v = 30$ mm/s. We note that along the bounded fault gouge, the pore fluid pressure increase might become negative. This is acceptable as long as the total pore fluid pressure doesn't become negative ($\Delta P(y, t) > -P_0$). This is a characteristic that also exists in our fully nonlinear numerical analyses on the bounded domain (see Stathas and Stefanou (2022), Figure ??).

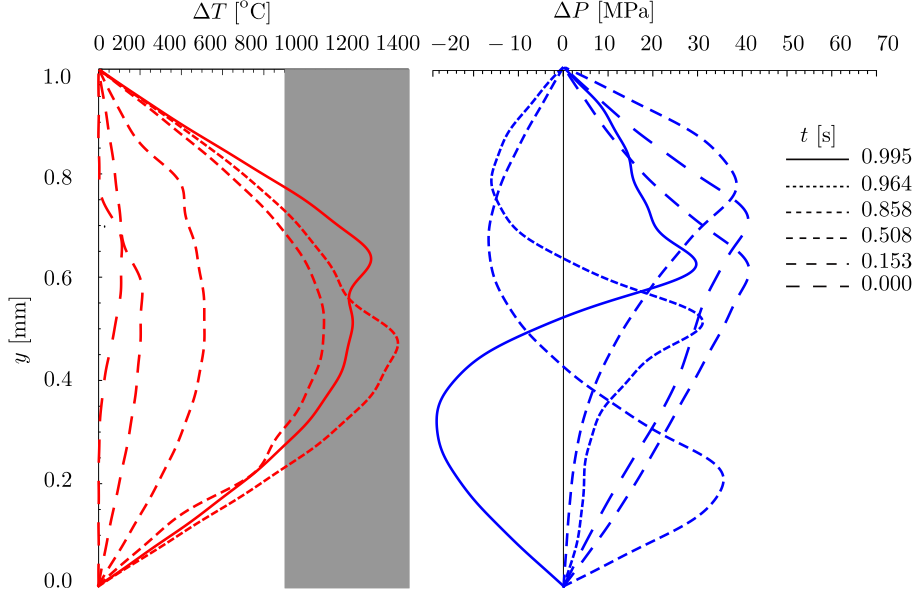


Figure 16: Temperature ΔT and pore fluid pressure ΔP fields along the height of the layer for shearing velocity $\dot{\delta} = 1$ m/s, at different times during the analysis. Because of the thermal load moving inside the domain closer to the sinks at the boundaries, temperature reaches markedly smaller values than in the stationary case. We note that the change in the pressure field presents negative values leading to regions of smaller pressure than the initial P_0 ($P(y, t) = P_0 + \Delta P(y, t)$). This coincides with the numerical analyses presented in Part I, Stathas and Stefanou (2022).

5. Conclusions

In this paper a series of numerical results have been obtained for the coupled thermal and pore fluid pressure diffusion equations. We follow the methodology developed in Rice (2006a); Rempel and Rice (2006), and we expand it to the cases of bounded domains and moving thermal loads resulting from traveling (flutter) instabilities on a Cauchy continuum (see Rice, 2006a; Benallal and Comi, 2003; Benallal, 2005; Rice et al., 2014b; Platt et al., 2014a).

To handle the integral differential equations the SCLM method was applied (see Elnagar and Kazemi, 1996; Tang et al., 2008). The method can handle the weakly singular kernels that appear in the unbounded case and the stationary thermal load on the bounded case. The method can also generalize to the case of a periodic traveling strain localization inside the bounded domain, which is in accordance with the numerical results of Part I, Stathas and Stefanou (2022).

It is found that contrary to the case of a stationary thermal load on an unbounded domain described in Rice (2006a), taking into account the existence of the boundary conditions at the edges of the fault gouge plays an important role at the frictional evolution of the fault for a range of values of the seismic slip velocities commonly observed during earthquake events. Namely, for a seismic slip δ of 1 m under a seismic slip velocity $\dot{\delta}=1$ m/s, the influence of the boundaries becomes important after the first 0.1 m of slip. It is shown that under the influence of homogeneous Dirichlet conditions on the bounded domain, a steady state is reached for the temperature field, which in turn implies that the effects of thermal pressurization progressively attenuate until it completely ceases. In this case the temperature rise inside the fault gouge is well above the melting point of the fault gouge material. The apparent

scarcity of pseudodactilites and absence of widespread melting observations in faults (see Brantut et al. (2008); Kanamori and Brodsky (2004a); Rice (2006a)), however, indicates that other possible frictional weakening mechanisms will become prevalent, such as chemical decomposition of minerals (see Sulem and Famin, 2009).

Furthermore, the effects of a moving thermal load corresponding to a traveling strain localization (flutter instability) inside the fault gouge, were examined under both unbounded and bounded boundary conditions. In both cases, traveling strain localization mode showed the existence of a plateau in the frictional strength of the fault, τ_{res} (see Figures 8, 13).

In the case of the traveling load on the unbounded domain, the fact that the load changes its position constantly leads to a non zero change of the temperature field ($\frac{\partial \Delta T(x,t)}{\partial t} \neq 0$) and constant influence of the pore fluid pressure profile by the thermal pressurization term. Moreover, because the thermal load changes its position, temperature does not have time to accumulate in one point and provoke a pressure increase that eliminates fault friction. Instead fault friction reaches a non-zero plateau (see Figure 8). This is an important result since it directly influences the dissipation energy produced during seismic slip.

Moreover, we examined the influence of the velocity of the strain localization (moving thermal load) in the frictional evolution. Based on our analyses, we established that the faster traveling shear bands have a smoother stress drop at the first stages of the analysis and they reach a higher plateau of frictional strength, see Figure 10. When the velocity of the shear band tends to zero we retrieve the solution described in Rice (2006a), as expected.

Next, a traveling instability was applied into a bounded domain with homogeneous Dirichlet boundary conditions. Again the results show that the frictional strength of the fault reaches a plateau and is not fully recovered as in the case of a stationary instability (see Figure 13). The reason is the change of the position of the thermal load during the analysis and the subsequent change of the temperature profile, leading to a non attenuating thermal pressurization phenomenon. Again the plateau reached, differs based on the traveling velocity of the shear band v , which ranges in the order of $20 \sim 50$ mm/s according to the numerical analyses of Part I, Stathas and Stefanou (2022). In this case, it is shown that in contrast to the case of a stationary thermal load on the bounded domain, the fault never recovers entirely its frictional strength since the effects of thermal pressurization never cease.

The results presented above clearly show a strong dependence of the fault's frictional behavior in both the fault gouge boundary conditions and the strain localization mode (traveling or stationary PSZ) introduced into the medium. These results can be used as a preliminary model in order to evaluate qualitatively the results obtained by numerical analyses taking into account the microstructure of the fault gouge material, where discerning between the effects of the different mechanisms affecting the frictional response of a fault undergoing thermal pressurization is more involved. The results of the fully non-linear numerical analyses with the Cosserat micromorphic continuum of Part I agree qualitatively with the results from the linear model of this paper. This indicates that the driving cause behind the obtained results is the diffusion from the thermal and hydraulic couplings. The microstructure follows to a lesser extend. Its use in the solution of the BVP presented in Part I (see Stathas and Stefanou (2022)), is required in order for the dissipation and the meta-stable frictional response of the fault gouge to be calculated correctly excluding mesh dependency from the numerical results.

In conclusion, our results show that for typical values of seismic slip δ and seismic slip velocity $\dot{\delta}$, the effects of the boundaries of the fault gouge cannot be ignored. This means that those effects need to be accounted in both numerical analyses and laboratory experiments. The influence of different kind of boundary conditions needs to be studied. The introduction of a traveling (flutter-type) strain localization mode is an important aspect of our model. Its presence increases the frequency content of the earthquake and it prevents the bounded fault gouge from fully recovering its frictional shear strength due to the diffusion at the boundaries. Furthermore, it contributes in keeping the temperatures inside the fault gouge smaller than in the stationary cases. The existence of oscillations and the reduction of the peak residual frictional strength are also important in understanding the transition from a stable to unstable seismic slip and subsequent fault nucleation (see Rempel and Rice, 2006; Rice, 1973, 2006a; Viesca and Garagash, 2015, among others). Furthermore, the existence of non zero upper and lower bounds in the fault's frictional behavior (τ_{min}, τ_{res}), has serious implications for any attempt in control-

ing the transition from stable (aseismic) to unstable (coseismic) slip (see Stefanou, 2019; Stefanou and Tzortzopoulos, 2020; Tzortzopoulos, 2021).

Acknowledgments

The authors would like to acknowledge the support of the European Research Council (ERC) under the European Union's Horizon 2020 research and innovation program (Grant agreement no. 757848 CoQuake).

Appendix A. The coupled Thermo-hydraulic problem and its solution

Appendix A.1. Problem description

We have already discussed that we are interested in the limiting case where the position and profile of the PSZ can be prescribed inside the fault gouge. Knowing the form of the profile of the shear plastic strain-rate in $\dot{\gamma}^p(y, t)$ (equation (2)), the two way coupled problem in the form of temperature and pressure diffusion equations is given by:

- Heat diffusion BVP:

$$\begin{aligned} \frac{\partial \Delta T}{\partial t} &= c_{th} \frac{\partial \Delta T}{\partial y^2} + \frac{1}{\rho C} \tau(t) V \delta_{\text{Dirac}}(y - u(t)), \\ \Delta T \Big|_{y=0} &= \Delta T \Big|_{y=H} = 0, \\ \Delta T(y, 0) &= 0, \end{aligned} \tag{A.1}$$

where $T(y, t)$ is the unknown change in temperature in the fault gouge layer of height H . The fault gouge is considered to be in isothermal boundary conditions during shearing. The coupled pressure problem is given by:

- Pressure diffusion BVP, in its Homogeneous form:

$$\begin{aligned} \frac{\partial \Delta P}{\partial t} &= c_{hy} \frac{\partial \Delta P}{\partial y^2} + \Lambda \frac{\partial \Delta T}{\partial t}, \\ \Delta P \Big|_{y=0} &= \Delta P \Big|_{y=H} = \Delta P(y, t) - \Delta P(y, 0) = 0, \\ P(y, 0) &= P_0, \end{aligned} \tag{A.2}$$

where $\Delta P(y, t)$ is the unknown pressure difference between the fault gouge layer and the boundaries, while $P_0 = P(y, 0)$ is the initial pore fluid pressure, that is kept constant at the boundaries of the fault gouge (drained boundary conditions).

We note that the above formulations are also valid in the case of an unbounded domain considering $H \rightarrow \pm\infty$. The pressure problem affects also the temperature BVP through the value of shear stress (fault friction), $\tau(t)$, in the yielding region. According to the Mohr-Coulomb yield criterion, subtracting the initial ambient pore fluid pressure P_0 we get:

$$\tau(t) = f(\sigma_n - p_0) - f \Delta P_{max}(t). \tag{A.3}$$

We note here that once we know the form of the plastic strain-rate profile $\dot{\gamma}^p(y, t)$ as in equation (A.1) the only unknown is the fault friction $\tau(t)$. We can find the solution of the temperature equation $T(y, t)$ in terms of the unknown fault friction $\tau(t)$ and replace into the pressure equation, which can then also be described as an unknown function of friction. Finally, we can define the value of fault friction $\tau(t)$ by inserting the pressure increase solution $\Delta P(y, t)$ into the material equation (A.3) and solving for $\tau(t)$. The above equations have constant coefficients and since the loading is prescribed (based on the unknown $\tau(t)$), the system has been transformed to a one-way coupled set of linear differential 1D diffusion equations of the form:

$$\begin{aligned} \frac{\partial q(y, t)}{\partial t} &= c \frac{\partial^2 q(y, t)}{\partial x^2} + \frac{1}{k} g(y, t), \\ a_1 \frac{\partial u}{\partial n_1} \Big|_{y=0} + b_1 q \Big|_{y=0}(t) &= f_1(t), \quad t > 0, \\ a_2 \frac{\partial q}{\partial n_2} \Big|_{y=H} + b_2 u \Big|_{y=H}(t) &= f_2(t), \quad t > 0, \\ q(y, 0) &= I(y), \end{aligned} \tag{A.4}$$

where $q(y, t)$ is the unknown function (e.g. the temperature $T(y, t)$), f_i , $i = 1, 2$ are the values of the general Robin boundary conditions with coefficients $(a_i, b_i, i = 1, 2)$, $I(y)$ is the initial condition and $g(y, t)$ is the loading function (here related to frictional dissipation). We denote by c the diffusivity and by k the conductivity of the material.

Appendix A.2. Fundamental solution

We can find the solution to the above BVP by application of the Green's theorem, which for the general diffusion case in 1D reads (see Cole et al. (2010)):

$$q(y, t) = \int_0^H G(y, t; y', 0, c) I(y') dy' + \frac{c}{k} \int_0^t \int_0^H g(y', t') G(y, t; y', t', c) dy' dt' + c \int_0^t \sum_{i=1}^2 \left[\frac{f_i(t')}{a_i} G(y, t; y'_i, t', c) \right] dt' - \alpha \int_0^t \sum_{i=1}^2 \left[f_i(t') \frac{G(y_i, t; y', t', c)}{n'_i} \right]_{y'=y_i} dt', \quad (\text{A.5})$$

where $G(y, t; y', t', c)$ is the appropriate Green's function. The first two terms correspond to the initial condition $I(y, 0)$ and the loading term $g(y, t)$ respectively. The terms α, k represent the diffusivity and the conductivity of the unknown quantity $q(y, t)$ respectively. The third term is important for non homogeneous Neumann and Robin boundary conditions while the fourth term refers to non homogeneous Dirichlet boundary conditions. In what follows the last two terms in equation (A.5) are omitted due to the existence of homogeneous Dirichlet boundary conditions in the problems of temperature and pressure difference diffusion at hand.

Applying the solution in terms of the Green's function (A.5) to problems (A.1), (A.2) we obtain the solution in terms of the Green's function specific to each diffusion problem.

$$\Delta T(y, t) = \frac{c_{th}}{k_T} \int_0^t \int_{-\infty}^{\infty} g_T(y', t') G(y, t; y', t', c_{th}) dy' dt', \quad (\text{A.6})$$

$$\Delta P(y, t) = \frac{c_{hy}}{k_H} \int_0^t \int_{-\infty}^{\infty} g_H(y', t') G(y, t; y', t', c_{hy}) dy' dt', \quad (\text{A.7})$$

where c_{th}, k_T are the thermal diffusivity, conductivity pair and c_{hy}, k_H are their hydraulic counterparts. Similarly (g_T, g_H) are the loading functions, while $G(y, t; y', t', c)$ is the Green's function kernel for the thermal ($c = c_{th}$) and pressure ($c = c_{hy}$) diffusion problems respectively.

In the case of the coupled pressure problem (A.2) with the temperature as a loading function, we are interested in rewriting the system's response with the help of the dissipative loading $(\frac{1}{\rho C} \tau(t) \gamma^p)$ of the temperature equation (A.1). This way we can connect the pressure response $P(y, t)$ to the fault friction $\tau(t)$ which is the main unknown. We can do this by replacing in the expression of $T(y, t)$ in the pressure diffusion equation (A.2) the temperature impulse response of equation (A.1) due to a impulsive (Dirac) thermal load. This way the response obtained from the pressure diffusion equation is a Green's function kernel that contains the influence of an impulse thermal load (see Appendix Appendix B for detailed derivation in the cases of 1) a bounded domain for a stationary impulsive thermal load and 2) an unbounded domain subjected to a moving impulsive thermal load). The pressure solution can then be written as:

$$\Delta P(y, t) = P(y, t) - P_0 = \frac{\Lambda \dot{\delta}}{\rho C (c_{hy} - c_{th})} \int_0^t \int_{-\infty}^{\infty} g_T(y', t') G^*(y, t; y', t', c_{hy}, c_{th}) dy' dt', \quad (\text{A.8})$$

where $G^*(y, t; y', t', c_{hy}, c_{th})$ is the Green's function kernel of the pressure equation (A.2) containing the influence of an impulse thermal load from the temperature equation (A.1).

Having found the pressure solution $P(y, t)$ as a function of g_T we can then replace (A.8) into the material description equation (A.3). For the case of 1D shear τ under constant normal load σ_n that we will consider throughout this paper, the material law is transformed into the integral equation:

$$\tau(t) = f(\sigma_n - P_0) - C \int_0^t \int_{-\infty}^{\infty} g_T(y', t') G^*(y, t; y', t', c_{hy}, c_{th}) dy' dt', \quad (\text{A.9})$$

where $C = \frac{f\Lambda\delta}{\rho C(c_{hy} - c_{th})}$. Due to the concentrated nature of the thermal load (Dirac distribution), the integral equation (A.9) can be brought to its final form:

$$\tau(t) = f(\sigma_n - p_0) - C \int_0^t \tau(t') G^*(y, t; y', t', c_{hy}, c_{th}) \big|_{y=y'(t')} dt' \quad (\text{A.10})$$

The above integral equation is a linear Volterra integral equation of the second kind Wazwaz (2011). We note here that this equation is valid only at the position of the yielding plane which has to coincide with the position of the maximum pressure inside the layer ($y = y'(t')$). This has been proven to hold true for the cases present on the unbounded domain (see Appendix ??). In the case of a bounded fault gouge under the influence of a traveling PSZ (thermal load) this is true only in the regions again from the boundary. Nevertheless, the difference between the position of the traveling thermal load and that of the P_{max} is small (see also Figure 16).

Appendix B. Derivation of the coupled pore fluid pressure diffusion kernel.

In this appendix we derive the coupled pore fluid pressure diffusion kernel for the cases of a bounded domain subjected to a stationary Dirac load and an unbounded domain under a moving Dirac load. Our procedure follows the discussion in Lee and Delaney (1987) where the same problem was solved for a stationary Dirac thermal load on an unbounded domain.

Appendix B.1. Stationary thermal load, coupled pore fluid pressure Green's kernel for a bounded domain.

In the case of the bounded domain we proceed by applying the method of separation of variables and then expanding the solution to a Fourier series. We note here that the coupled system of pressure and temperature diffusion equations have the same form of linear partial differential operators and boundary conditions and therefore their solution belongs to the same space of Sturm-Liouville problems. In essence the two solutions have the same eigenfunctions. In the case of the bounded domain the Temperature diffusion equation has the solution given in Cole et al. (2010):

$$\Delta T(y, t) = \sum_{n=1}^{\infty} \frac{2}{H\rho C} \int_0^t \int_{-\infty}^{\infty} g(y', t') \exp[-\lambda_n^2 c_{th}(t - t')] \sin(\lambda_n x) \sin(\lambda_n y') dy' dt', \quad (\text{B.1})$$

where λ_n is the Sturm-Liouville eigenfunction coefficient, $\lambda_n = \frac{n\pi}{H}$, H is the length of the bounded domain. The eigencondition for the homogeneous Dirichlet boundary conditions are given by:

$$\sin\left(\frac{n\pi}{H}H\right) = 0, \quad \lambda_n = \frac{n\pi}{H}, \quad n = 1, 2, \dots \quad (\text{B.2})$$

We note here that the homogeneous pressure diffusion partial differential equation on the above bounded domain has the same boundary conditions. Therefore, the pore fluid pressure solution can be written with the same eigenfunctions as above. Replacing the pore fluid pressure eigenfunction expansion $\Delta P(x, t) = P(y, t) - P_0 = \sum_{n=1}^{\infty} \tilde{p}_n \sin \frac{n\pi x}{H}$ into the coupled pressure diffusion partial differential equation,

$$\begin{aligned} \frac{\partial \Delta P(y, t)}{\partial t} - c_{hy} \frac{\partial^2 \Delta P(y, t)}{\partial y^2} &= \Lambda \frac{\partial \Delta T(y, t)}{\partial t}, \\ \Delta P(y, 0) &= 0, \\ \Delta P(0, t) = \Delta P(H, t) &= 0, \end{aligned} \quad (\text{B.3})$$

we obtain:

$$\sum_{n=1}^{\infty} \frac{\partial \tilde{p}_n(t)}{\partial t} \sin \lambda_n y + c_{hy} \sum_{n=1}^{\infty} \lambda_n^2 \tilde{p}_n(t) \sin \lambda_n y = \frac{2\Lambda}{H\rho C} \sum_{n=1}^{\infty} \sin \lambda_n y \frac{\partial T_n(t)}{\partial t}, \quad (\text{B.4})$$

where $T_n(t)$ is given as:

$$T_n(t) = \int_0^t \int_{-\infty}^{\infty} g(y', t') \exp[-\lambda_n^2 c_{th}(t - t')] \sin \lambda_n y' dy' dt'.$$

Isolating each eigenfunction $\sin \lambda_n y$ we arrive at the following first order linear differential equations involving the unknown coefficient $\tilde{p}_n(t)$ and the loading coefficient $T_n(t)$ for each particular component of the solution series expansion.

$$\frac{\partial \tilde{p}_n(t)}{\partial t} + c_{hy} \lambda_n^2 \tilde{p}_n(t) = \frac{2\Lambda}{H\rho C} \frac{\partial T_n(t)}{\partial t}, \quad t \geq 0. \quad (\text{B.5})$$

Applying the Laplace transformation in the field of time:

$$s\tilde{P}_n(s) + c_{hy} \lambda_n^2 \tilde{P}_n(s) = \frac{2\Lambda}{H\rho C} \frac{s}{s + \lambda_n^2 c_{th}} \int_{-\infty}^{\infty} G(y', s) \sin \lambda_n y' dy'. \quad (\text{B.6})$$

$$\tilde{P}_n(s) = \frac{2\Lambda}{H\rho C} \frac{s}{(s + \lambda_n^2 c_{th})(s + \lambda_n^2 c_{hy})} \int_{-\infty}^{\infty} G(y', s) \sin \lambda_n y' dy' \quad (\text{B.7})$$

Applying the inverse of the Laplace transform gives us:

$$\tilde{p}_n(y, t) = \frac{2\Lambda}{H\rho C} \int_0^t \int_{-\infty}^{\infty} g(y', t') \frac{c_{hy} \exp[-\lambda_n^2 c_{hy}(t - t')] - c_{th} \exp[-\lambda_n^2 c_{th}(t - t')]}{c_{hy} - c_{th}} \sin \lambda_n y' dy' dt' \quad (\text{B.8})$$

Finally, in the series expansion $\Delta P(y, t) = \sum_{n=1}^{\infty} \tilde{p}_n(t) \sin \lambda_n y$ we move the summation under the integral sign and we obtain:

$$\Delta P(y, t) = \frac{2\Lambda}{H\rho C} \int_0^t \int_{-\infty}^{\infty} g(y', t') \sum_{n=1}^{\infty} \frac{c_{hy} \exp[-\lambda_n^2 c_{hy}(t - t')] - c_{th} \exp[-\lambda_n^2 c_{th}(t - t')]}{c_{hy} - c_{th}} \sin \lambda_n y \sin \lambda_n y' dy' dt' \quad (\text{B.9})$$

We recognize the term in the second line of equation (B.9) as the Green's function kernel of the coupled pressure diffusion partial differential equation. This expression has the added advantage that the influence of the thermal load on the pressure $\Delta P(y, t) = P(y, t) - P_0$ solution is straightforward. Noticing that for a general diffusion problem on a bounded domain under homogeneous Dirichlet boundary conditions the Green's function kernel is given by:

$$G_{X11}(y, t; y', t', c) = \frac{2}{H} \sum_{n=1}^{\infty} \exp\left[-\lambda_n^2 c \frac{t - t'}{H^2}\right] \sin \lambda_n y \sin \lambda_n y'. \quad (\text{B.10})$$

The Green's function kernel of the coupled pressure differential equation on the bounded domain is then given as:

$$G_{X11}(y, t; y', t', c_{th}, c_{hy}) = \frac{c_{hy} G_{X11}(y, t; y', t', c_{hy}) - c_{th} G_{X11}(y, t; y', t', c_{th})}{c_{hy} - c_{th}}. \quad (\text{B.11})$$

Finally, the pressure solution can be given as:

$$\Delta P(y, t) = P(y, t) - P_0 = \frac{\Lambda}{\rho C} \int_0^t \int_{-\infty}^{\infty} g(y', t') G_{X11}(y, t; y', t', c_{th}, c_{hy}) dy' dt' \quad (\text{B.12})$$

This result agrees with the formula provided in Lee and Delaney (1987); Rice (2006a) for the unbounded domain.

Appendix B.2. Moving thermal load, coupled pore fluid pressure Green's kernel for a unbounded domain.

Here, we present the derivation of the Green's function kernel of the coupled pressure diffusion equation for an unbounded domain under moving thermal load. Note here, that the Green's function kernel is independent of the type of loading (stationary or moving), it depends on the kind of the differential operator and the boundary conditions. What differs here in the form of the Green's function kernel is the velocity dependence, since we want to connect the pressure evolution not with the stationary Green's function but with the moving Dirac thermal load, that can be written as $g(y, t) = \frac{\dot{\delta}}{\rho C} \tau(t) \delta(y - vt)$. In essence we need to only prescribe the velocity dependence of $x' = f(v, t')$ in the Green's function kernel for the unbounded domain under Dirichlet conditions $G_{X00}(y, t; y', t', c_{hy}, c_{th})$. We provide a full

description and then compare the results. The coupled system of temperature and pore fluid pressure diffusion equations in the unbounded domain is given by:

$$\begin{aligned}
\frac{\partial \Delta T(y, t)}{\partial t} - c_{th} \frac{\partial^2 \Delta T(y, t)}{\partial y^2} &= \frac{\dot{\delta}}{\rho C} \tau(t) \delta(y - vt), \quad -\infty < y < \infty, \quad 0 < t < \infty \\
\frac{\partial \Delta P(y, t)}{\partial t} - c_{hy} \frac{\partial^2 \Delta P(y, t)}{\partial y^2} &= \Lambda \frac{\partial \Delta T(y, t)}{\partial t}, \quad -\infty < y < \infty, \quad 0 < t < \infty, \\
\Delta T(y, 0) &= 0, \\
\lim_{y \rightarrow -\infty, y \rightarrow \infty} \Delta T(y, t) &= 0, \\
\Delta P(y, 0) &= 0, \\
\lim_{y \rightarrow -\infty, y \rightarrow \infty} \Delta P(y, t) &= 0
\end{aligned} \tag{B.13}$$

To account for the moving load we perform a change of variables on the original system (B.13), setting $\xi = y - vt$, $\eta = t$ so that we attach a frame of reference to the moving load. In this case and by suitable application of the chain rule we can write:

$$\begin{aligned}
\frac{\partial \Delta T(\xi, \eta)}{\partial \eta} - v \frac{\partial \Delta T}{\partial \xi} - c_{th} \frac{\partial^2 \Delta T(\xi, \eta)}{\partial \xi^2} &= \frac{1}{\rho C} \tau(\eta) \delta(\xi), \quad -\infty < \xi < \infty, \quad 0 < \eta < \infty, \\
\frac{\partial \Delta P(\xi, \eta)}{\partial \eta} - v \frac{\partial \Delta P(\xi, \eta)}{\partial \xi} - c_{hy} \frac{\partial^2 \Delta P(\xi, \eta)}{\partial \xi^2} &= \Lambda \frac{\partial \Delta T(\xi, \eta)}{\partial \eta}, \quad -\infty < \xi < \infty, \quad 0 < \eta < \infty \\
\Delta T(\xi, 0) &= 0, \\
\lim_{\xi \rightarrow -\infty, \xi \rightarrow \infty} \Delta T(\xi, \eta) &= 0, \\
\Delta P(\xi, 0) &= 0, \\
\lim_{\xi \rightarrow -\infty, \xi \rightarrow \infty} \Delta P(\xi, \eta) &= 0
\end{aligned} \tag{B.14}$$

Applying a Fourier transform in space and a Laplace transform in time on the system of partial differential equations (B.14) we obtain:

$$\begin{aligned}
s\tilde{T}(k, s) - v(ik)\tilde{T}(k, s) - c_{th}(ik)^2\tilde{T}(k, s) &= \frac{1}{\rho C} \tau(s), \\
s\tilde{P}(k, s) - v(ik)\tilde{P}(k, s) - c_{th}(ik)^2\tilde{P}(k, s) &= \Lambda s\tilde{T}(k, s).
\end{aligned} \tag{B.15}$$

Solving the above algebraic system (B.15) we obtain:

$$\tilde{T}(k, s) = \frac{1}{\rho C} \frac{\tau(s)}{s - v(ik) + c_{th}k^2}, \tag{B.16}$$

$$\tilde{P}(k, s) = \frac{\Lambda \tau(s)}{\rho C} \frac{s}{(s - v(ik) + c_{th}k^2)(s - v(ik) + c_{hy}k^2)} \tag{B.17}$$

Inverting the Laplace and then the Fourier transform yields:

$$\begin{aligned}
\Delta T(y, t) &= \frac{\dot{\delta}}{\rho C} \int_0^t \frac{\tau(t')}{2\sqrt{\pi c_{th}(t - t')}} \exp \left[-\frac{(y - vt')^2}{4c_{th}(t - t')} \right] dt', \\
\Delta P(y, t) &= \frac{\Lambda \dot{\delta}}{\rho C(c_{hy} - c_{th})} \int_0^t \frac{\tau(t')}{2\sqrt{\pi(t - t')}} \left(\sqrt{c_{hy}} \exp \left[-\frac{(y - vt')^2}{4c_{hy}(t - t')} \right] - \sqrt{c_{th}} \exp \left[-\frac{(y - vt')^2}{4c_{th}(t - t')} \right] \right) dt'.
\end{aligned} \tag{B.18}$$

By inspection we note that these are the same expressions as the ones presented in (9), where y' was replaced by $y' = vt'$ and $c = c_{th}$, or $c = c_{hy}$ respectively.

Appendix C. Collocation Methodology

Appendix C.1. Regular kernels

In order to apply the collocation methodology to the linear Volterra integral equation of the second kind, (15), we make use of the collocation methodology described in Tang et al. (2008). The integral equation

is given as:

$$\bar{\tau}(\bar{t}) = 1 - C \int_0^{\bar{t}} \bar{\tau}(\bar{t}') \bar{G}^*(\bar{y}, \bar{t}; \bar{y}', \bar{t}') \|_{\bar{y}=\bar{y}'} d\bar{t}', \quad \bar{t} \in [0, T \frac{c_{th}}{H^2}], \quad (C.1)$$

where $\bar{T} = T \frac{c_{th}}{H^2}$ is the final normalized time, and $\bar{\tau}(\bar{t})$ is the unknown function. We begin by performing a change of variables from $\bar{t} \in [0, \bar{T}]$ to $\bar{z} \in [-1, 1]$. The change of variables reads:

$$\bar{t} = \bar{T} \frac{1 + \bar{z}}{2}, \quad \bar{z} = \frac{2\bar{t}}{\bar{T}} - 1$$

The Volterra integral equation can then be written:

$$U(\bar{z}) = 1 - C \int_0^{\bar{T} \frac{1+\bar{z}}{2}} \bar{G}^*(\bar{y}, \bar{T} \frac{1+\bar{z}}{2}; \bar{y}', \bar{t}') \|_{\bar{y}=\bar{y}'} d\bar{t}', \quad \bar{z} \in [-1, 1], \quad (C.2)$$

where $U(\bar{z}) = \tau(\bar{T} \frac{1+\bar{z}}{2})$. In order for the collocation method solution to converge exponentially we require that both the integral equation (C.2) and the integral inside (C.2) are expressed inside the same interval $[-1, 1]$. To do this first we change the integration bounds from $\bar{t}' \in [0, \bar{T} \frac{1+\bar{z}}{2}]$ to $s \in [-1, \bar{z}]$.

$$U(\bar{z}) = 1 - C \int_0^{\bar{z}} K(\bar{y}, \bar{z}; \bar{y}', s) \|_{\bar{y}=\bar{y}'} U(s) ds, \quad \bar{z} \in [-1, 1], \quad (C.3)$$

where $K(\bar{y}, \bar{z}; \bar{y}', s) = \frac{\bar{T}}{2} \bar{G}^*(\bar{y}, \frac{\bar{T}}{2}(\bar{z} + 1); \bar{y}', \frac{\bar{T}}{2}(s + 1))$. Next, we set the $N + 1$ collocation points $\bar{z}_i \in [-1, 1]$ and corresponding weights ω_i according to the Clenshaw-Curtis quadrature formula. The integral equation (C.3) must hold at each \bar{z}_i :

$$U(\bar{z}_i) = 1 - C \int_0^{\bar{z}_i} K(\bar{y}, \bar{z}_i; \bar{y}', s) \|_{\bar{y}=\bar{y}'} U(s) ds, \quad i \in [0, N], \quad (C.4)$$

The main hindrance in solving equation (C.4) accurately, is the calculation of the integral with variable integration bounds. For small values of \bar{z}_i , the quadrature provides little information for $U(s)$. We handle this difficulty by yet another variable change where we transfer the integration variable $s \in [-1, \bar{z}_i]$ to $\theta \in [-1, 1]$ via the transformation:

$$s(\bar{z}, \theta) = \frac{1 + \bar{z}}{2} \theta + \frac{\bar{z} - 1}{2}, \quad \theta \in [-1, 1]. \quad (C.5)$$

Thus, equation (C.4) is transformed into:

$$U_i + C \frac{1 + \bar{z}_i}{2} \sum_{j=0}^N u_j \sum_{p=0}^N K(\bar{y}, \bar{z}_i; \bar{y}', s(\bar{z}_i, \theta)) \|_{\bar{y}=\bar{y}'} U(s(\bar{z}_i, \theta_p)) \omega_j = 1, \quad i \in [0, N] \quad (C.6)$$

In order to apply the collocation method according to the Clenshaw-Curtis quadrature, we express the solution $U(s(\bar{z}_i, \theta_p))$ with the help of Lagrange interpolation polynomials $P_j(s(\bar{z}_i, \theta_p))$ as a series:

$$U(s(\bar{z}_i, \theta_p)) \sim \sum_{k=0}^N u_j P_j(s(\bar{z}_i, \theta_p)),$$

$$U_i + \frac{1 + \bar{z}_i}{2} \sum_{j=0}^N u_j \left(\sum_{p=0}^N K(\bar{y}, \bar{z}_i; \bar{y}', s(\bar{z}_i, \theta)) \|_{\bar{y}=\bar{y}'} P_j(s(\bar{z}_i, \theta_p)) \omega_p \right) = 1, \quad i \in [0, N] \quad (C.7)$$

where, $P_j(s(\bar{z}_i, \theta_p))$, $\sum_{j=0}^N u_j$ have been defined in the main text (see equations (21) and (22)). In order to assure an exponential degree of convergence, we choose the set of Gauss Chebyshev quadrature points for the numerical evaluation of the integral $\{\theta_j\}_{j=0}^N$, to coincide with the set of collocation points $\{\bar{z}_j\}_{j=0}^N$, where the integral equation is evaluated. Rearranging the terms and applying Einstein's summation over repeated indices yields the system of algebraic equations:

$$(\delta_{ij} + A_{ij}) U_j = g(\bar{z}_i), \quad (C.8)$$

where, $A_{ij} = \frac{1 + \bar{z}_i}{2} \sum_{j=0}^N u_j \left(\sum_{p=0}^N K(\bar{y}, \bar{z}_i; \bar{y}', s(\bar{z}_i, \theta)) P_j(s(\bar{z}_i, \theta_p)) \omega_p \right)$, $g(\bar{z}_i) = 1$ and U_j the unknown quantities. Because Lagrange interpolation was assumed, the interpolation coefficients U_j calculated at each \bar{x}_j are also the value of the interpolation at \bar{z}_j .

Appendix C.2. Singular kernels

When the kernel of the integral equation (15) involves a singularity (see equation (16)), we cannot use the Clenshaw-Curtis quadrature rule in its original form because the quadrature requires the values of the function at a position, where the kernel evaluates to infinity. For this reason a different quadrature strategy needs to be implemented. Here, based on the work of Tang et al. (2008) we apply the Gauss-Chebyshev quadrature rule. This quadrature rule involves the values of the function at the zeros of the N -th degree Chebyshev polynomial of the first kind $\{\bar{z}'_i\}$. The quadrature can then be successfully calculated, because the new set of integration points, $\{\bar{z}'_i\}$, does not involve the ends of the interval $[-1,1]$. However, since the Chebyshev polynomials of the first kind were used, we need to take into account the specific weight function $w(\bar{z}) = \sqrt{1 - \bar{z}^2}$ under which the Chebyshev polynomials of the first kind are orthogonal on the interval $[-1,1]$, namely:

$$\int_{-1}^1 \frac{T_i(\bar{z})T_j(\bar{z})}{\sqrt{1 - \bar{z}^2}} d\bar{z} = \begin{cases} 1, & i = j \\ 0, & i \neq j \end{cases}, \quad (\text{C.9})$$

moreover, due to the change in the evaluation set, $\{\bar{z}'_i\}$, the formula for the calculation of the Lagrange interpolation is given by:

$$U(s(\bar{z}, \theta_p)) = \sum_{j=0}^N U(\bar{z}'_j) F_j(s(\bar{z}, \theta_p)) \quad (\text{C.10})$$

where $F_j(s(\bar{z}, \theta_p))$ are the Lagrange cardinal polynomials. We note that the formula for the Lagrange cardinal polynomials changes due to the change of the interpolation nodes $\{\bar{z}'_j\}_{j=0}^N$. Taking advantage of the orthogonality condition the cardinal polynomials $F_j(s(\bar{z}, \theta_p))$ are given by:

$$F_j(s(\bar{z}'_i, \theta_p)) = \sum_{p=0}^N \alpha_{p,j} T_p(s(\bar{z}'_i, \theta_p)), \quad (\text{C.11})$$

where, again due to orthogonality, $\alpha_{p,j}$ is given by:

$$\alpha_{p,j} = T_p(\bar{z}'_j) \omega_j / \gamma_p, \quad (\text{C.12})$$

$$\gamma_p = \begin{cases} \pi, & j = 0 \\ \frac{\pi}{2}, & j \neq 0 \end{cases} \quad (\text{C.13})$$

The final discretized form of the integral equation (15) is then given by:

$$U_i + \frac{1 + \bar{z}_i}{2} \sum_{j=0}^N U_j \left(\sum_{p=0}^N K(y, \bar{z}_i; \bar{y}', s(\bar{z}_i, \theta)) \|_{\bar{y}=\bar{y}'} F_j(s(\bar{z}_i, \theta_p)) \sqrt{1 - \theta_p^2} \omega_p \right) = 1, \quad i \in [0, N]. \quad (\text{C.14})$$

we note here that the term $\sqrt{1 - \theta_p^2}$, accounts for the weight function present in the orthogonality condition.

References

- Aki, K., 1967. Scaling law of seismic spectrum. *Journal of Geophysical Research* 72, 1217–1231. doi:10.1029/jz072i004p01217.
- Andrews, D.J., 2005. Rupture dynamics with energy loss outside the slip zone. *Journal of Geophysical Research: Solid Earth* 110, 1–14. doi:10.1029/2004JB003191.
- Aydin, A., 2000. Fractures, faults, and hydrocarbon entrapment, migration and flow. *Marine and petroleum geology* 17, 797–814.
- Badt, N.Z., Tullis, T.E., Hirth, G., Goldsby, D.L., 2020. Thermal Pressurization Weakening in Laboratory Experiments. *Journal of Geophysical Research: Solid Earth* 125, 1–21. doi:10.1029/2019JB018872.

-
- Benallal, A., 2005. On localization modes in coupled thermo-hydro-mechanical problems. *Comptes Rendus Mécanique* 333, 557–564. doi:<https://doi.org/10.1016/j.crme.2005.05.005>.
- Benallal, A., Comi, C., 2003. Perturbation growth and localization in fluid-saturated inelastic porous media under quasi-static loadings. *Journal of the Mechanics and Physics of Solids* 51, 851–899. doi:10.1016/S0022-5096(02)00143-6.
- Boyd, J., 2006. 2000. chebyshev and fourier spectral methods. Dover, New York. .
- Brantut, N., Schubnel, A., Rouzaud, J.N., Brunet, F., Shimamoto, T., 2008. High-velocity frictional properties of a clay-bearing fault gouge and implications for earthquake mechanics. *Journal of Geophysical Research: Solid Earth* 113, 1–18. doi:10.1029/2007JB005551.
- Brauer, F., Nohel, J., 1969. *The Qualitative Theory of Ordinary Differential Equations: An Introduction*. Dover Publications, New York.
- Brown, J.W., Churchill, R.V., et al., 2009. *Complex variables and applications*. Boston: McGraw-Hill Higher Education.
- Brune, J.N., 1970. Tectonic stress and the spectra of seismic shear waves from earthquakes. *J Geophys Res* 75, 4997–5009. doi:10.1029/jb075i026p04997.
- Carslaw, H.S., Jaeger, J.C., 1959. *Conduction of heat in solids*. Technical Report. Clarendon Press.
- Churchill, R.V., 1972. *Operational mathematics* .
- Cole, K., Beck, J., Haji-Sheikh, A., Litkouhi, B., 2010. *Heat conduction using Greens functions*. CRC Press.
- Collins-Craft, N.A., Stefanou, I., Sulem, J., Einav, I., 2020. A cosserat breakage mechanics model for brittle granular media. *Journal of the Mechanics and Physics of Solids* , 103975.
- Elnagar, G.N., Kazemi, M., 1996. Chebyshev spectral solution of nonlinear Volterra-Hammerstein integral equations. *Journal of Computational and Applied Mathematics* 76, 147–158. doi:10.1016/S0377-0427(96)00098-2.
- Evans, G.A., Hyslop, J., Morgan, A.P., 1981. Iterative solution of Volterra integral equations using Clenshaw-Curtis quadrature. *Journal of Computational Physics* 40, 64–76. doi:10.1016/0021-9991(81)90199-6.
- Griffani, D., Rognon, P., Metzger, B., Einav, I., 2013. How rotational vortices enhance transfers. *Physics of Fluids* 25, 093301.
- Harbord, C., Brantut, N., Spagnuolo, E., Toro, G.D., 2021. Fault friction during simulated seismic slip pulses .
- Kanamori, H., Brodsky, E.E., 2004a. The physics of earthquakes. *Reports on Progress in Physics* 67, 1429–1496. URL: <https://doi.org/10.1088/2F0034-4885/2F67/2F8/2Fr03>, doi:<https://doi.org/10.1088/0034-4885/67/8/r03>.
- Kanamori, H., Brodsky, E.E., 2004b. The physics of earthquakes. *Reports on Progress in Physics* 67, 1429–1496. doi:10.1088/0034-4885/67/8/R03.
- Kanamori, H., Rivera, L., 2006. Energy partitioning during an earthquake. *Geophysical Monograph Series* 170, 3–13. doi:10.1029/170GM03.
- Koepf, W., 1999. Efficient computation of chebyshev polynomials in computer algebra. *Computer Algebra Systems: A Practical Guide* , 79–99.
- Lachenbruch, A.H., 1980. Frictional heating, fluid pressure, and the resistance to fault motion. *Journal of Geophysical Research: Solid Earth* 85, 6097–6112. doi:<https://doi.org/10.1029/JB085iB11p06097>.
- Lee, T.C., Delaney, P.T., 1987. Frictional heating and pore pressure rise due to a fault slip. *Geophysical Journal of the Royal Astronomical Society* 88, 569–591. doi:10.1111/j.1365-246X.1987.tb01647.x.
- Lyapunov, A., 1893. On the problem of stability of motion. *Stability of Motion* 30, 123–127.

-
- Mase, C.W., Smith, L., 1984. Pore-fluid pressures and frictional heating on a fault surface. *Pure and Applied Geophysics* PAGEOPH 122, 583–607. doi:10.1007/BF00874618.
- Mase, C.W., Smith, L., 1987. Effects of frictional heating on the thermal, hydrologic, and mechanical response of a fault. *Journal of Geophysical Research* 92, 6249–6272. doi:10.1029/JB092iB07p06249.
- Mavaleix-Marchessoux, D., Bonnet, M., Chaillat, S., Leblé, B., 2020. A fast BEM procedure using the Z-transform and high-frequency approximations for large-scale 3D transient wave problems. *International Journal for Numerical Methods in Engineering* .
- Miller, T., Rognon, P., Metzger, B., Einav, I., 2013. Eddy viscosity in dense granular flows. *Physical review letters* 111, 058002.
- Muhlhaus, H.B., Vardoulakis, I., 1988. The thickness of shear bands in granular materials. *Géotechnique* 38, 331–331. doi:10.1680/geot.1988.38.2.331b.
- Myers, R., Aydin, A., 2004. The evolution of faults formed by shearing across joint zones in sandstone. *Journal of Structural Geology* 26, 947–966.
- Nicchio, M.A., Nogueira, F.C., Balsamo, F., Souza, J.A., Carvalho, B.R., Bezerra, F.H., 2018. Development of cataclastic foliation in deformation bands in feldspar-rich conglomerates of the rio do peixe basin, ne brazil. *Journal of Structural Geology* 107, 132–141. doi:https://doi.org/10.1016/j.jsg.2017.12.013.
- Passelègue, F.X., Goldsby, D.L., Fabbri, O., 2014. The influence of ambient fault temperature on flash-heating phenomena. *Geophysical Research Letters* 41, 828–835.
- Platt, J.D., Rudnicki, J.W., Rice, J.R., 2014a. Stability and localization of rapid shear in fluid-saturated fault gouge: 2. Localized zone width and strength evolution. *Journal of Geophysical Research: Solid Earth* 119, 4334–4359. doi:10.1002/2013JB010711.
- Platt, J.D., Rudnicki, J.W., Rice, J.R., 2014b. Stability and localization of rapid shear in fluid-saturated fault gouge: 2. localized zone width and strength evolution. *Journal of Geophysical Research: Solid Earth* 119, 4334–4359. doi:https://doi.org/10.1002/2013JB010711.
- Quarteroni, A., Sacco, R., Saleri, F., 2007. *Numerical Mathematics Texts in Applied Mathematics*.
- Rattez, H., Stefanou, I., Sulem, J., 2018. The importance of Thermo-Hydro-Mechanical couplings and microstructure to strain localization in 3D continua with application to seismic faults. Part I: Theory and linear stability analysis. *Journal of the Mechanics and Physics of Solids* 115, 54–76. URL: https://doi.org/10.1016/j.jmps.2018.03.004, doi:10.1016/j.jmps.2018.03.004.
- Rempe, M., Di Toro, G., Mitchell, T.M., Smith, S.A., Hirose, T., Renner, J., 2020. Influence of Effective Stress and Pore Fluid Pressure on Fault Strength and Slip Localization in Carbonate Slip Zones. *Journal of Geophysical Research: Solid Earth* 125. doi:10.1029/2020JB019805.
- Rempel, A., 2006. The effects of flash-weakening and damage on the evolution of fault strength and temperature. *Earthquakes: Radiated energy and the physics of faulting* 170, 263–270.
- Rempel, A.W., Rice, J.R., 2006. Thermal pressurization and onset of melting in fault zones. *Journal of Geophysical Research: Solid Earth* 111. doi:10.1029/2006JB004314.
- Rice, J.R., 1973. The growth of slip surfaces in the progressive failure of over-consolidated clay. *Proceedings of the Royal Society of London. A. Mathematical and Physical Sciences* 332, 527–548. doi:10.1098/rspa.1973.0040.
- Rice, J.R., 1975. On the stability of dilatant hardening for saturated rock masses. *Journal of Geophysical Research* 80, 1531–1536. doi:10.1029/jb080i011p01531.
- Rice, J.R., 2006a. Heating and weakening of faults during earthquake slip. *Journal of Geophysical Research: Solid Earth* 111, 1–29. doi:10.1029/2005JB004006.
- Rice, J.R., 2006b. Heating and weakening of faults during earthquake slip. *Journal of Geophysical Research: Solid Earth* 111. doi:https://doi.org/10.1029/2005JB004006.

-
- Rice, J.R., Rudnicki, J.W., Platt, J.D., 2014a. Stability and localization of rapid shear in fluid-saturated fault gouge: 1. linearized stability analysis. *Journal of Geophysical Research: Solid Earth* 119, 4311–4333. doi:<https://doi.org/10.1002/2013JB010710>.
- Rice, J.R., Rudnicki, J.W., Platt, J.D., 2014b. Stability and localization of rapid shear in fluid-saturated fault gouge: 1. Linearized stability analysis. *Journal of Geophysical Research: Solid Earth* 119, 4311–4333. doi:10.1002/2013JB010710.
- Rognon, P., Miller, T., Einav, I., 2015. A circulation-based method for detecting vortices in granular materials. *Granular Matter* 17, 177–188.
- Sibson, R., 1977. Fault rocks and fault mechanisms. *Journal of the Geological Society* 133, 191–213.
- Sibson, R.H., 2003. Thickness of the Seismic Slip Zone. *Bulletin of the Seismological Society of America* 93, 1169–1178. URL: <https://doi.org/10.1785/0120020061>, doi:10.1785/0120020061.
- Stathas, A., Stefanou, I., 2022. Fault friction under thermal pressurization during large coseismic-slip part i: Numerical analyses. - -, -.
- Stefanou, I., 2019. Controlling Anthropogenic and Natural Seismicity: Insights From Active Stabilization of the Spring-Slider Model. *Journal of Geophysical Research: Solid Earth* 124, 8786–8802. doi:10.1029/2019JB017847.
- Stefanou, I., Tzortzopoulos, G., 2020. Control instabilities and incite slow-slip in generalized burridge-knopoff models. arXiv:2008.03755 URL: <https://arxiv.org/abs/2008.03755>, arXiv:2008.03755.
- Sulem, J., Famin, V., 2009. Thermal decomposition of carbonates in fault zones: Slip-weakening and temperature-limiting effects. *Journal of Geophysical Research: Solid Earth* 114, 1–14. doi:10.1029/2008jb006004.
- Sulem, J., Stefanou, I., 2016. Thermal and chemical effects in shear and compaction bands. *Geomechanics for Energy and the Environment* 6, 4–21. URL: <http://dx.doi.org/10.1016/j.gete.2015.12.004>, doi:10.1016/j.gete.2015.12.004.
- Sulem, J., Stefanou, I., Veveakis, E., 2011. Stability analysis of undrained adiabatic shearing of a rock layer with cosserat microstructure. *Granular Matter* 13, 261–268. doi:<https://doi.org/10.1007/s10035-010-0244-1>.
- Sulem, J., Vardoulakis, I., Ouffroukh, H., Boulon, M., Hans, J., 2004. Experimental characterization of the thermo-poro-mechanical properties of the aegion fault gouge. *Comptes Rendus Geoscience* 336, 455–466.
- Tanaka, H., Chen, W., Kawabata, K., Urata, N., 2007. Thermal properties across the chelungpu fault zone and evaluations of positive thermal anomaly on the slip zones: Are these residuals of heat from faulting? *Geophysical Research Letters* 34.
- Tang, T., Xu, X., Cheng, J., 2008. On spectral methods for volterra integral equations and the convergence analysis. *Journal of Computational Mathematics* , 825–837.
- Trefethen, L.N., 2019. *Approximation Theory and Approximation Practice*, Extended Edition. SIAM.
- Tzortzopoulos, G., 2021. Controlling earthquakes in the laboratory using pertinent fault stimulating techniques.
- Vardoulakis, I., 1985. Stability and bifurcation of undrained, plane rectilinear deformations on water-saturated granular soils. *International journal for numerical and analytical methods in geomechanics* 9, 399–414.
- Vardoulakis, I., 1996a. Deformation of water-saturated sand: I. uniform undrained deformation and shear banding. *Géotechnique* 46, 441–456.
- Vardoulakis, I., 1996b. Deformation of water-saturated sand: II. effect of pore water flow and shear banding. *Géotechnique* 46, 457–472.